














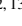



Trends in Silicates in the β Pictoris Disk

Cicero X. Lu ¹, Christine H. Chen ^{1,2}, B. A. Sargent ^{1,2}, Dan M. Watson ³, Carey M. Lisse ⁴, Joel D. Green ²,
Michael L. Sitko ^{5,6}, Tushar Mittal ⁷, V. Leboutteiller ⁸, G. C. Sloan ^{9,10}, Isabel Rebolledo ², Dean C. Hines ², Julien H. Girard ²,
Michael W. Werner ¹¹, Karl R. Stapelfeldt ¹¹, Winston Wu ^{12,13} and Kadin Worthen ¹

¹Department of Physics and Astronomy, The Johns Hopkins University, 3400 N. Charles Street, Baltimore, MD 21218, USA

²Space Telescope Science Institute, 3700 San Martin Dr., Baltimore, MD 21218, USA

³Department of Physics and Astronomy, University of Rochester, 500 Wilson Blvd, Rochester, NY 14627, USA

⁴Johns Hopkins University Applied Physics Laboratory, 11100 Johns Hopkins Rd, Laurel, MD 20723, USA

⁵Department of Physics, University of Cincinnati, Cincinnati, OH 45221, USA

⁶Space Science Institute, Boulder, CO 80301, USA

⁷MIT Department of Earth, Atmospheric, and Planetary Sciences, Green Bldg, The 77 Massachusetts Ave, Cambridge, MA 02139, USA

⁸AIM, CEA, CNRS, Université Paris-Saclay, Université Paris Diderot, Sorbonne Paris Cité, F-91191 Gif-sur-Yvette, France

⁹Space Telescope Science Institute, 3700 San Martin Drive, Baltimore, MD 21218, USA

¹⁰Department of Physics and Astronomy, University of North Carolina, Chapel Hill, NC 27599-3255, USA

¹¹Jet Propulsion Laboratory, California Institute of Technology, 4800 Oak Grove Drive, Pasadena, CA 91107, USA

¹²Center for Language and Speech Processing, Department of Computer Science, Johns Hopkins University, Baltimore, MD 21218, USA

¹³Computer Science and Engineering, University of Michigan, Ann Arbor, MI 48109, USA

(Received Nov 19, 2021; Accepted May 16, 2022)

Abstract

While β Pic is known to host silicates in ring-like structures, whether the properties of these silicate dust vary with stellocentric distance remains an open question. We re-analyze the β Pictoris debris disk spectrum from the *Spitzer* Infrared Spectrograph (IRS) and a new IRTF/SpeX spectrum to investigate trends in Fe/Mg ratio, shape, and crystallinity in grains as a function of wavelength, a proxy for stellocentric distance. By analyzing a re-calibrated and re-extracted spectrum, we identify a new $18\ \mu\text{m}$ forsterite emission feature and recover a $23\ \mu\text{m}$ forsterite emission feature with a substantially larger line-to-continuum ratio than previously reported. We find that these prominent spectral features are primarily produced by small submicron-sized grains, which are continuously generated and replenished from planetesimal collisions in the disk and can elucidate their parent bodies' composition. We discover three trends about these small grains: as stellocentric distance increases, (1) small silicate grains become more crystalline (less amorphous), (2) they become more irregular in shape, and (3) for crystalline silicate grains, the Fe/Mg ratio decreases. Applying these trends to β Pic's planetary architecture, we find that the dust population exterior to the orbits of β Pic b and c differs substantially in crystallinity and shape. We also find a tentative $3\text{--}5\ \mu\text{m}$ dust excess due to spatially unresolved hot dust emission close to the star. From our findings, we infer that the surfaces of large planetesimals are more Fe-rich and collisionally-processed closer to the star but more Fe-poor and primordial farther from the star.

Unified Astronomy Thesaurus concepts: Debris disks (363); Planetary system formation (1257); Silicate grains (1456); Exoplanet formation (492); Planetesimals (1259); Exo-zodiacal dust (500); Spectroscopy (1558); Infrared astronomy (786)

1. Introduction

Debris disks are planetary systems that contain dust, planetesimals, planets, and gas (Hughes et al. 2018), and they provide important insights into planet formation. Theoretical models suggest that two main mechanisms efficiently remove dust grains. Stellar radiation pressure removes grains smaller than the so-called “blowout size” from debris disks

cicerolu@jhu.edu

Corresponding author: Cicero X. Lu

(Dent et al. 2014), while it causes the μm -to-mm grains to drift towards their star via the Poynting-Robertson (P-R) effect (Guess 1962). However, debris disks are observed to be dust-rich, containing grains with a wide range of sizes from sub- μm to several millimeters in diameter. The presence of sub-blowout size grains in observations points to an active dust replenishing mechanism: collisions among parent bodies such as planetesimals, asteroids, and/or unseen planets. The *Spitzer Space Telescope* has revealed signatures of such collisional activities in the mid-infrared wavelengths through spectroscopy, imaging, and time-series photometry (Chen et al. 2020).

The properties of small dust grains in debris disks, such as crystallinity and Fe-to-Mg abundance, inform us about properties of their larger parent bodies and offer a direct comparison with asteroids and Kuiper Belt Objects (KBOs) in the Solar System. In the Solar System, asteroidal and cometary relic planetesimals are abundant with crystalline silicates (Lisse et al. 2006, 2007; Brownlee 2008; Reach et al. 2010; Wooden et al. 2017). Specifically, comets that originate from the Trans-Neptunian region contain Mg-rich silicates (Wooden et al. 2017), whereas asteroids and chondrites originating from the asteroid belt are Fe-rich (Le Guillou et al. 2015). Similar to the Solar System, a significant fraction ($\sim 25\%$) of debris disks are also found to contain crystalline silicate grains (Chen et al. 2014; Mittal et al. 2015). However, most of these disks are too far to be spatially resolved, and thus we cannot map the crystallinity or Fe-to-Mg ratio in these disks.

As one of the few nearby (20 pc) systems that can be spatially resolved by existing telescopes, β Pic provides us with the opportunity to compare its dust distributions and properties with Solar System dust grain distributions and properties. β Pictoris (β Pic) is a 20 Myr old A-type dwarf star and hosts dust, planetesimals, gas and at least two planets (Lagrange et al. 2009, 2010, 2020; Nowak et al. 2020). Ground-based mid-infrared spectra and images of the β Pic disk have revealed mid-infrared (MIR) thermal emission attributed to amorphous and crystalline silicate species (Weinberger et al. 2003; Telesco et al. 2005). These silicate species display distinct spatial structures (Okamoto et al. 2004). Specifically, high angular resolution spectroscopy with Subaru COMICS has shown that the crystalline silicates are located towards the center of the disk, and sub- μm -sized amorphous silicates are distributed in three concentric rings (Okamoto et al. 2004; Wahhaj et al. 2003). However, ground-based MIR observations are inherently limited by the sky thermal background and are unable to resolve regions beyond 30 AU from the star, missing the majority of the disk that spans out to 1400 AU in the *Spitzer* Multiband Imaging Photometer (MIPS) $24\ \mu\text{m}$ image (Ballering et al. 2016) and 1800 AU in the scattered light image (Larwood & Kalas 2001).

Space-based mid and far-infrared (FIR) observations enable both the discovery and characterization of cool crystalline silicates in the far out regions of the β Pic disk that are inaccessible to ground-based observations. The *Spitzer* Infrared Spectrograph (IRS) has detected forsterite emission bands at 28 and $33.5\ \mu\text{m}$, indicating a cool crystalline silicate population (Chen et al. 2007). The *Herschel* Space Observatory’s FIR Photodetector Array Camera and Spectrometer (PACS) has revealed a separate population of cool crystalline forsterite through the $69\ \mu\text{m}$ forsterite band. These silicates has been found to have a Mg/Fe ratio of 99 : 1 (de Vries et al. 2012). Such a Mg-rich silicate grain composition suggests that the parent bodies, planetesimals are primitive and unprocessed, similar to the comets seen in the Kuiper Belt in our Solar System.

Since the β Pic debris disk contains multiple populations of silicates, our goal is to investigate whether there are any trends in dust properties as a function of wavelength. In this work, we re-extract the β Pic *Spitzer* IRS spectrum using Advanced Optimal extraction (AdOpt) (Lebouteiller et al. 2010) and re-analyze the silicate properties in the spectrum. In addition, we measure the $0.7\text{--}3\ \mu\text{m}$ spectrum with the NASA Infrared Telescope facility (IRTF) SpeX to better constrain the stellar properties. In section 2, we describe the IRTF observations and the re-reduction of the *Spitzer* IRS observations. In section 3, we present our photosphere modeling. In section 4, we describe our modeling of the photosphere-subtracted thermal continuum and silicate emission features in detail. In Section 5, we analyze the abundance of dust grain species and the trends in grain properties. In Section 6, we discuss the implications of trends in grain properties. We conclude our paper in Section 7.

2. Observations

2.1. SPEX

We observe the β Pic system using NASA’s Infrared Telescope Facility (IRTF) Medium Resolution Spectrograph and Imager (SpeX) in its Short wavelength cross-dispersed (SXD) ($R\sim 2000$, $0.7\text{--}2.55\ \mu\text{m}$) and Long wavelength cross-dispersed (LXD) ($R\sim 2500$, $1.7\text{--}5.5\ \mu\text{m}$) modes (Rayner et al. 2003) on 2021 February 02 at 05:47:18 UT and 07:12:12 UT. We use nearby (within 0.5 deg and 0.1 in airmass) HD 37781 (A0V, $K = 6.516$) as a calibration standard to measure the atmospheric effects on our observations of β Pic. We observe β Pic and HD 37781 in SXD mode with a total on-target integration time of 92s and 180 s, and in LXD mode for a total on-target integration time of 66 s and 637 s respectively, at an airmass ~ 3 . Both stars are observed in ABBA nod mode for telescope and sky background removal.

We reduce our data using Spextool v4.1 (Cushing et al. 2004; Vacca et al. 2003). The calibrated β Pic SXD spec-

trum has a signal-to-noise ratio (SNR) of 100–300, similar to that of the calibrator HD 37781. However, although the β Pic LXD has SNR of 100–300, most regions in the calibrator’s LXD has SNR of < 1 , due to insufficient on-target integration time (calibrator is ~ 4 mags fainter than β Pic). As a result, the calibrated β Pic spectrum has $\text{SNR} \geq 10$ only at wavelengths 1.7–2.55 and 3.0–4.0 μm . The region in between these windows is heavily impacted by the atmospheric transmission window.

We perform absolute flux calibration of the IRTF SXD spectrum using ESO VLT/NACO JHK photometry (Bon-
nefoy et al. 2013). First, we calculate the synthetic photometry F_J^{SXD} , F_H^{SXD} , and F_K^{SXD} by convolving the SXD spectrum with NACO JHK’s filter transmission functions. Next, we calculate a scaling factor

$$C_{\text{SXD}} = \frac{F_J^{\text{SXD}} + F_H^{\text{SXD}} + F_K^{\text{SXD}}}{F_J^{\text{NACO}} + F_H^{\text{NACO}} + F_K^{\text{NACO}}}. \quad (1)$$

We calculate a scaling factor C_{SXD} of 1.04, indicating that the F^{SXD} for JHK bands are on average 4% dimmer than F^{NACO} for JHK bands. This 4% difference is within the IRTF SpeX instrumental accuracy (5%, Rayner et al. 2003). Therefore, we multiply the IRTF SpeX spectrum by 1.04 to be consistent with NACO photometry data. The SNR of the LXD spectrum is limited by the SNR of the standard star and thus suffers from a $\sim 30\%$ loss in brightness compared to the L’ band photometry. In addition, the LXD spectrum is heavily impacted by the atmospheric transmission. Therefore, we do not perform any further analysis on the LXD spectrum.

2.2. *Spitzer* IRS

We re-extract and re-calibrate the *Spitzer* IRS (Houck et al. 2004) low-resolution β Pic spectrum (originally published in Chen et al. 2007) with the most up-to-date IRS extraction and calibration tools (Lebouteiller et al. 2010). In the original β Pic spectrum, Chen et al. (2007) discovered the 23 and 35 μm crystalline silicate emission bands. However, their spectrum displays “sawtooth” fringing patterns as a result of detector artifacts that were not able to be corrected for at the time. With advancements in both *Spitzer* science center pipelines and knowledge of empirical Point Spread Functions (PSFs), we now attempt to minimize those detector artifacts that could mask astrophysical signals. In the following subsections, we describe in detail our procedures for re-extracting and re-calibrating the β Pic observations.

IRS is a MIR spectrograph that covers 5.2 – 38 μm with low ($R \sim 60 - 130$) and moderate ($R \sim 600$) resolution spectroscopic capabilities, and has two operating modes: a mapping mode and a staring mode. For our work, we focus on low-resolution observations of β Pic. The low resolution mode consists of two modules, Short-Low (SL) and Long-Low (LL). Both have three grating orders with two main orders SL1, SL2, LL1, LL2 and a short “bonus” order (SL3,

LL3). Since SL3 (LL3) is observed simultaneously with the SL1 (LL1) and shares the same observation setups, we omit a separate description of SL3 (LL3). β Pic is observed with a combination of mapping mode and staring mode. See Table 1 for details. All low resolution observations are made with the spectrograph long slit aligned along the position angle of β Pic disk to within 15° . We describe details in the following subsections.

2.2.1. β Pic Observations using the IRS Mapping Mode

During SL2, SL3, SL1, and LL2 observations, *Spitzer* mapped the vertical extent of the disk by stepping the telescope across the disk at a specific number of positions (# Pointings in Table 1), each separated by 1.8'' except for LL2 (2.1'' for LL2). Because the slits are long and narrow (Slit Size), the disk is only fully captured in the slit in the central map position (Pointing Extracted), where the star is well centered in the slit in the dispersion direction. Figure 1 shows a cartoon of three SL2 pointings including the central pointing (exposure 6). In the rest of the pointings, the midplane of the disk is outside of the slit and results in low SNR. Thus, we only perform analysis on the central pointing.

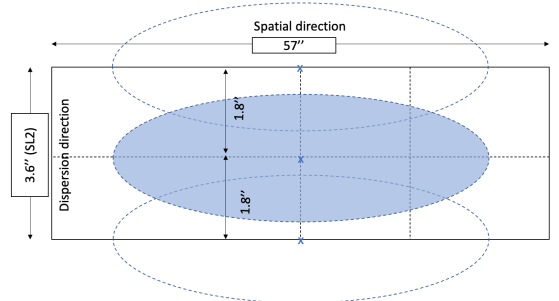


Figure 1. A cartoon illustration of the position of the β Pic disk with respect to the SL slit ($57'' \times 3.6''$ slit) for the IRS SL1 and SL2 mapping mode observations. The telescope was stepped across the β Pic disk in the dispersion direction in increments of 1.8'' with the disk well-centered in the central pointing as illustrated by the shaded ellipse. The pointings represented by the dotted empty ellipses are not centered in the dispersion direction. The LL2 observations follow similar mapping patterns, where only the central pointing is well-centered in the dispersion direction. Drawing not to scale.

For well-centered exposures, we compare slit sizes with the size of β Pic disk and determine the effect of telescope PSF on SL and LL observations to ensure that the disk is completely captured in the slit. Since *Spitzer* is diffraction-limited, the PSF scales as $1.22 \lambda/D$, where D is the diameter of *Spitzer*’s mirror and λ is the wavelength. For SL observations, the PSF is 1.5'' (1 pixel) at 5 μm and 4.4'' (2.5 pixel) at 15 μm . For LL observations, the PSF is 4.4'' (0.9 pixel)

Table 1. Observation setup

Order	Wavelength (μm)	Mode	Date	AOR Key	# Pointings	Pointing Extracted	Slit Size	Plate scale ($''/\text{pix}$)
SL2	5.2–7.7	Mapping	2004 Nov 16	9872288	7	Exp 4	$57'' \times 3.7''$	1.8
SL3	7.3–8.7	Mapping	2004 Nov 16	8972544	11	Exp 6	$57'' \times 3.6''$	1.8
SL1	7.4–14.5	Mapping	2004 Nov 16	9872288	11	Exp 6	$57'' \times 3.6''$	1.8
LL2	13.9–21.3	Mapping	2005 Feb 9	9016832	5	Exp 3	$168'' \times 10.5''$	5.1
LL3	19.4–21.7	Staring	2005 Feb 9	9016832	2	Exp 1, 2	$168'' \times 10.7''$	5.1
LL1	19.9–38.0	Staring	2004 Feb 4	9016064	2	Exp 1, 2	$168'' \times 10.7''$	5.1

Notes. “SL” stands for Short-Low module and “LL” stands for Long-Low module. See Figure 1 for a visualization of mapping mode dither patterns.

at $15 \mu\text{m}$ and $10.4''$ (2 pixel) at $35 \mu\text{m}$. We find that the β Pic disk roughly spans 3 pixels (approximately $15''$) $15 \mu\text{m}$ in the radial direction and therefore the slits are long enough to capture the entire disk. We also find that disk is spatially resolved in both SL and LL and plan to publish the spatially-resolved IRS spectra of the β Pic disk in a subsequent paper. We measure the misalignment angle between the LL slit position angle ($\text{PA}_{\text{slit}} = 44.97 \pm 0.02^\circ$) and disk midplane PA ($\text{PA}_{\text{disk}} = 29.51^\circ$) to be 15° . We overlay the IRS LL2 slit on top of the data for a visualization (see Appendix Figure A1). We conclude that the minor misalignment does not affect the observation such that the entire disk is captured in the well-centered exposures.

We re-extract SL1,2,3 and LL2 spectra with Advanced Optimal extraction (AdOpt, [Lebouteiller et al. 2010](#)). AdOpt first uses empirical super-sampled PSFs to simultaneously fit the PSF to all of the pixels in the spatial direction of the slit and determine weights for individual pixels. In doing so, AdOpt weights the pixels in the extraction window by their SNR and position on the detector to measure the flux at every wavelength. We do not observe any obvious effects of fringing in the extracted SL1,2,3, and LL2 spectra and therefore do not apply fringing correction.

2.2.2. β Pic Observations using the IRS Staring Mode

The β Pic LL1 and LL3 spectra were observed with IRS staring mode, which stepped the disk at two nod positions (equivalent to pointings) at one-third (Nod 1) and two-thirds (Nod 2) along the slit. First, we extract the spectrum from each nod position with AdOpt. β Pic is well-centered in the dispersion direction of the slit in Nod 1 but not well-centered in Nod 2. The flux in Nod 2 is 20% lower across all wavelengths than in Nod 1. For the IRS staring mode, the AdOpt supports user-input extraction positions. Therefore, we use the manual optimal extraction option in SMART ([Lebouteiller et al. 2010](#)) to adjust the extraction position on the detector plane. We test offset position values between -1

and $+1$ in 0.1 increments. We find that an extraction offset (offset = -0.39 pixels) best matches the radial profile for the detector image by minimizing the residual, (the difference between between the data and extraction profile) across all LL1 wavelengths. After manually extracting the Nod 2 spectrum, we find that the flux between Nod 1 and Nod 2 spectra are consistent with one another to within $\leq 1\%$.

We find artifacts from fringing in LL1 spectra and corrected for them by using an empirical Relative Spectral Response Function (RSRF) to correct for out-of-slit light losses. The calibrator star’s RSRF spectrum for is defined as the model photosphere divided by the empirical spectrum and therefore characterizes the detector artifacts across pixels. We construct a one-dimensional RSRF for the LL1 wavelength range using a standard K giant star, ξ Dra. ξ Dra was observed on 2005 February 12 (AOR key 13195008) as a part of the IRS calibration program ([Sloan et al. 2015](#)). Since ξ Dra is very bright in the mid IR (7 Jy at $15 \mu\text{m}$) and has no observed infrared excess, its spectrum is approximately a bare stellar photosphere. We divide out a normalized ξ Dra IRS spectrum from the β Pic spectrum for the RSRF correction. The fringe-correction is effective in removing the fringing effects (e.g., bumps and wiggles) from the spectrum.

2.3. Absolute Flux Calibration and Order Stitching

We perform absolute flux calibration by pinning the LL1 spectrum to the MIPS $24 \mu\text{m}$ flux using LL1 as an anchoring order to calibrate the rest of LL and SL spectra. First, we perform our own MIPS $24 \mu\text{m}$ aperture photometry extraction by measuring the flux of the unresolved point source in the MIPS $24 \mu\text{m}$ image. We cannot use existing MIPS $24 \mu\text{m}$ photometry reported in [Ballerling et al. \(2016\)](#) as AdOpt’s extraction window differs from that used by [Ballerling et al. \(2016\)](#). AdOpt weights the extraction for the pixels by their SNR and their relative position on the detector. In doing so, AdOpt emphasizes the contribution from the high SNR unresolved point source. Specifically, we cal-

culate the MIPS $24\ \mu\text{m}$ flux, $F_{24\ \mu\text{m},\text{MIPS}}$ that is consistent with an unresolved point source, using aperture photometry with a radius of $3.5''$. We use the IDL-based tool, Image Display Paradigm #3 (IDP3) (Lytle et al. 1999) with background subtraction and aperture correction. We choose an annulus with an inner radius of $30''$ and an outer radius of $30.5''$ from disk center as the background, because the disk attenuates out to roughly $30''$ (Ballering et al. 2016). Next, we multiply our extracted flux by 2.57, the aperture correction given in the MIPS Instrument Handbook for a $3.5''$ aperture. We estimate $F_{24\ \mu\text{m},\text{IRS}}$, the synthetic photometry from the IRS spectrum. We convolve the MIPS $24\ \mu\text{m}$ filter response function with the IRS spectrum. For the unresolved central point source, we estimate the $F_{24\ \mu\text{m},\text{MIPS}} = 6.66$ Jy and the $F_{24\ \mu\text{m},\text{IRS}} = 7.01$ Jy. Therefore, we apply a scaling factor $C_{\text{IRS}} = F_{24\ \mu\text{m},\text{IRS}}/F_{24\ \mu\text{m},\text{MIPS}} = 0.95$ to the IRS observations to make them consistent with the MIPS $24\ \mu\text{m}$ observations. We report this scaling factor and any subsequent ones in the ‘‘Scaling Factor’’ column in Table 2 and photometry data in Table 3.

We use flux-calibrated LL1 spectrum as an anchoring spectrum to scale the rest of LL and SL spectra in descending wavelength order. There is an overlapping wavelength range (column ‘‘Overlapping Wavelength’’ in Table 2) between every two adjacent orders (column ‘‘Ref. Order or Photometry’’ in Table 2). To calibrate the flux in an order, we take the data points in its overlapping wavelength range with its reference order and calculate an average flux, f_{order} . We repeat this procedure for its reference order and obtain $f_{\text{ref. order}}$. Then, we take the ratio of the two to be the scaling factor $C_{\text{order}} = f_{\text{ref. order}}/f_{\text{order}}$. Specifically, take LL3 for an example, LL3 and LL1 overlaps between $19.9\text{--}21.7\ \mu\text{m}$. The scaling factor is $C_{\text{LL3}} = \sum_{19.9\ \mu\text{m}}^{21.7\ \mu\text{m}} f_{\text{LL1}}(\lambda) / \sum_{19.9\ \mu\text{m}}^{21.7\ \mu\text{m}} f_{\text{LL3}}(\lambda) = 1.12$. We report the rest of scaling factors in Table 2. Finally, we check our absolute flux calibration for the entire IRS spectrum with WISE photometry and we show that our absolute flux calibration is consistent with WISE in Fig. 2.

2.3.1. IRS spectrum Uncertainties

We take separate approaches to determine uncertainties for staring mode and mapping mode observations of the β Pic. For orders observed in IRS Staring mode (LL1 and LL3), we take the absolute value of the difference in flux between the two nod positions as the uncertainty of the spectra. For orders observed in IRS Mapping mode (SL1, SL2 and LL2 orders), we fit polynomials to part of the spectrum that are not affected by solid state features. We select regions at $5.6\text{--}7.9$ and $14.32\text{--}14.83\ \mu\text{m}$ of the spectrum and measure the root mean square (rms) of the spectrum from the polynomial fit. We assign the rms as the uncertainty for the spectrum if the

rms is bigger than 1% and adopted a 1% error floor according to Higdon et al. (2004). The resulting spectrum is shown in Fig. 2.

3. Analysis

In this section, we first describe fitting our new IRTF spectrum and existing photometry with stellar photosphere models to better predict the stellar photospheric emission at mid-infrared wavelengths. We then report our discovery of new silicate emission features from AdOpt extraction. Lastly, we describe our discovery of an infrared excess at $3\text{--}5\ \mu\text{m}$, consistent with the presence of hot dust in the system.

3.1. Stellar Photosphere

We model the β Pic stellar photosphere to understand (1) the relative flux contribution of disk emission to the overall brightness at the shortest wavelength in IRS β Pic spectrum and (2) to rigorously determine the overall shape of the disk emission spectrum. At H-band, Very Large Telescope Interferometer (VLTI) measurements suggest that the β Pic disk emission only constitutes 0.88% of the total emission (Ertel et al. 2014). Similarly, at the shortest wavelengths of the IRS spectrum ($5.3\ \mu\text{m}$), the spectrum is expected to be dominated by the stellar photosphere. We use the VLTI measurement to accurately estimate the brightness of the stellar photosphere at the shortest IRS wavelengths.

To predict the stellar photosphere at $5.5\ \mu\text{m}$, we fit β Pic’s UBVRJHK_s photometry (Table 3) and IRTF spectrum from $0.7\text{--}2.5\ \mu\text{m}$ with BT-NextGen models (Allard et al. 2012; Hauschildt et al. 1999). The addition of an IRTF β Pic spectrum better constrains the model’s spectral slope in the infrared wavelength range. β Pic has an edge-on disk, and therefore the disk might provide a small amount of extinction along line-of-sight. Therefore, we assume that extinction, E(B-V), is a free parameter and redden photosphere models using the general extinction law with $R_v = 3.1$ with ‘‘dust Extinction’’ software. We also include the effect of stellar rotation and limb darkening by convolving photosphere models with a line spread function consistent with $v \sin i = 130\ \text{km} \cdot \text{s}^{-1}$ (Claret 2000) and applying a limb-darkening coefficient of 0.24 consistent with the H band measurements of β Pic (Claret et al. 1995). Our best-fit model has $T_{\text{eff}} = 8000\text{K}$, $R_v = 3.1$, $A_v = 0.078$, $\log g = 4.0$ and $[M/H] = 0.0$ with a reduced $\chi^2 = 0.012$. Our best fit values for $\log g$, metallicity and the T_{eff} are consistent with those reported in the literature (e.g., Pecaut & Mamajek 2013). We note that this fit incorporates extinction as a free parameter for the first time. In figure 2, we show the β Pic stellar photosphere model, the IRTF spectrum and the *Spitzer* IRS spectrum together.

Next, we subtract off our best-fit stellar photosphere model from the IRS AdOpt spectrum. In figure 3, we plot the photosphere subtracted AdOpt spectrum of the unresolved point

Table 2. Absolute Flux Calibration Parameters

Order	Wavelength (μm)	Ref. Order or Photometry	Overlapping Wavelength	Scaling Factor (C_{order})
LL1	19.9–38.0	MIPS24	...	0.95
LL3	19.4–21.7	LL1	19.9–21.7	1.12
LL2	13.9–21.3	LL3	19.4–21.3	1.18
SL1	7.4–14.5	LL2	13.9–14.5	1.35
SL3	7.3–8.7	SL1	7.4–8.7	1.0
SL2	5.2–7.7	SL3	7.3–7.7	1.07

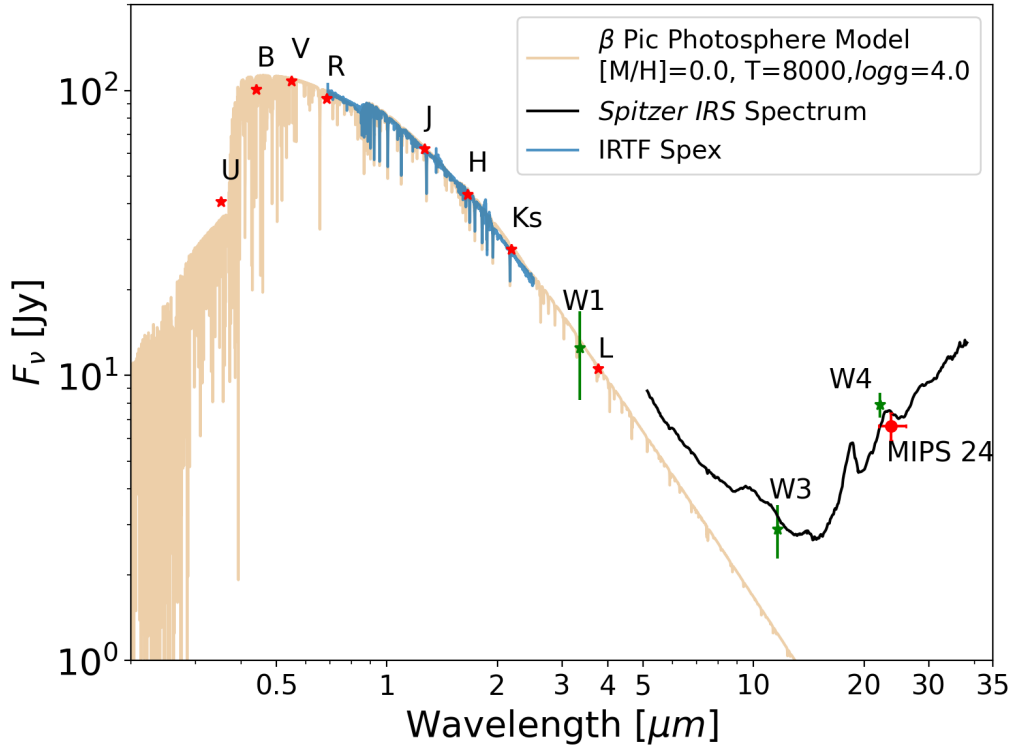


Figure 2. β Pic SED showing our best-fit model for the stellar photosphere overlaid on UBVJRJK_s photometry (see Table 3) and our 0.7–2.5 μm IRTF spectrum. Our best-fit model has $[M/H] = 0.0$, $T_{\text{eff}} = 8000\text{K}$, $\log g = 4$, $A_v = 0.078$ and $R_V = 3.1$. The red stars indicate photometry used in the stellar photosphere fitting, and the red circle is the MIPS 24 μm flux derived here for the unresolved central point source. The horizontal error bars indicate the FWHM of the band width for the MIPS 24 μm filter. The L band photometry indicates that the disk has no infrared excess at 3.77 μm . We omit W2 photometry because it is unreliable for sources brighter than magnitude of 5.

source in blue and the [Chen et al. \(2007\)](#) full-slit extraction spectrum in black for comparison. We can see the change in extraction window sizes brings out a new spectral feature at 18.5 μm and recovers the 23.7 μm crystalline forsterite feature previous reported in [Chen et al. \(2007\)](#) with a higher line-to-continuum ratio.

3.2. Discovery of the new spectral features

We discover an 18.5 μm spectral feature. We attribute the discovery of a new 18.5 μm feature to advancements in the knowledge of empirical *Spitzer* PSFs ([Sloan et al. 2015](#); [Lebouteiller et al. 2010](#)). These improvements enable us to (1) extract a spectrum with high SNR in the slit and (2) correct for fringing in the spectrum to further validate the fidelity of the new spectral feature using all of the calibration data obtained during the cryogenic mission. Specifically, compared

Table 3. Photometric Measurements of β Pic

Filter	Effective Wavelength Midpoint λ_{eff} for standard filters	Magnitude	Flux	Reference
	(μm)	(mag)	(Jy)	
U	0.3518	4.13 ± 0.01	40.6 ± 0.4	(a)
B	0.4407	4.03 ± 0.01	100.9 ± 1.0	(a)
V	0.5479	3.86 ± 0.01	108.0 ± 1.1	(a)
R	0.6864	3.74 ± 0.03	93.4 ± 2.6	(b)
J	1.265	3.524 ± 0.009	62.4 ± 0.75	(c)
H	1.66	3.491 ± 0.009	43.2 ± 0.4	(c)
K_s	2.18	3.451 ± 0.009	27.8 ± 0.3	(c)
L	3.77	3.454 ± 0.03	10.6 ± 0.03	(d)
W1	3.35	3.484 ± 0.4	12.5 ± 4.3	(e)
W3	11.6	2.597 ± 0.3	2.9 ± 0.6	(e)
W4	22.1	0.014 ± 0.016	7.9 ± 0.8	(f)
MIPS24 (Full Disk)	23.7	...	7.28 ± 0.73	(g)
IRS 24 (Unresolved Point Source)	23.7	...	7.01 ± 0.7	This Work
MIPS24 (Unresolved Point Source)	23.7	...	6.66 ± 0.67	This Work

Notes. (a). The General Catalogue of Photometric Data (GCPD) [Mermilliod et al. \(1997\)](#) (b). [Ducati \(2002\)](#) (c). [Bonnefoy et al. \(2013\)](#) (d). [Bouchet et al. \(1991\)](#) (e). AllWISE Source Catalog [Wright et al. \(2010\)](#); [Mainzer et al. \(2011\)](#); [Cutri & et al. \(2012\)](#). Note: W1 and W2 have 24% pixels saturated and W3 has 8% of pixels saturated. The saturation affect measurements precision as reflected in the inflated errorbars. (f). [Morales et al. \(2012\)](#) (g). [Su et al. \(2006\)](#); [Ballering et al. \(2016\)](#). We exclude W2 photometry because for source brighter than magnitude of 5, W2 photometry becomes unreliable.

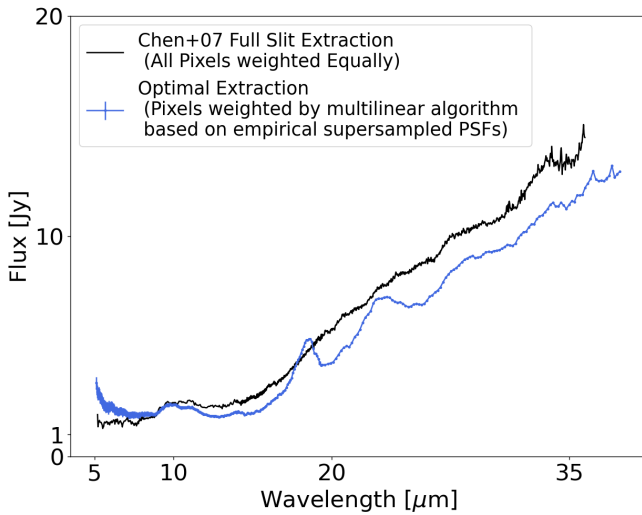


Figure 3. The β Pic IRS spectrum showcasing the newly discovered $18\mu\text{m}$ feature and a $23\mu\text{m}$ feature with larger line-to-continuum ratio that previously reported by [Chen et al. \(2007\)](#). The optimal extraction (this work) is in blue, while the full slit extraction published in [Chen et al. \(2007\)](#) is in black. The uncertainties for the spectrum extracted with AdOpt are on average at 1% level. The Chen+07 spectrum reduced using a full slit extraction has fringes.

to the [Chen et al. \(2007\)](#)'s full slit extraction, which weights every pixel in the entire slit equally, our AdOpt spectrum emphasizes the region close to the star. As the SNR increases towards the central star, most of the data points in our spectrum has less than 1% uncertainties.

We conclude that $18\mu\text{m}$ feature must be astrophysical and is emitted by dust grains in the disk. For the newly discovered $18\mu\text{m}$ feature, we verify that it is not a detector artifact by examining the entire IRS calibrator star library for LL2 observations to understand detector characteristics. Most fringing patterns only spans only 2 to a few (usually 5) data points but our $18\mu\text{m}$ feature has a FWHM of $\sim 2\mu\text{m}$ that spans more than 30 data points. More importantly, we do not see any $18\mu\text{m}$ artifacts in the calibrator star spectra that resemble our new $18\mu\text{m}$ feature. Therefore, we rule out the possibility that the $18\mu\text{m}$ arise from detector artifacts.

3.3. Constraints on the Spatial Distribution of the New $18\mu\text{m}$ Feature

Next, to constrain the spatial distribution of dust grains that are responsible the $18\mu\text{m}$ and $23\mu\text{m}$ spectral features, we analyze the Gemini Thermal-Region Camera Spectrograph (T-ReCS) spatially-resolved broadband MIR images

of β Pic disk (Telesco et al. 2005). Telesco et al. (2005) took image of the β Pic disk in Qa (central wavelength at $18.3\mu\text{m}$) and Qb (central wavelength at $24.6\mu\text{m}$) bands. In these broadband MIR images, both the disk continuum emission and the characteristic solid-state emission from dust contribute to the flux. As Qa and Qb bandpass’s wavelength range ($17.57\text{--}19.08$ and $23.62\text{--}25.54\mu\text{m}$) overlaps with our IRS solid-state emission features ($18.5\mu\text{m}$ and $23.8\mu\text{m}$), these MIR images can constrain the spatial distributions of the dust grains responsible for the solid state features. The T-ReCS images are diffraction-limited with beam sizes of $0.356''$ (7 AU) at $18.3\mu\text{m}$ and $0.445''$ (9 AU) at $24.6\mu\text{m}$, respectively, much finer than that of the Spitzer IRS. Therefore to include the effect of the changing PSF size with wavelength, we convolve the $18.3\mu\text{m}$ image with the a PSF profile at $24.6\mu\text{m}$, such that when we take the ratio of two images in subsequent analysis, the PSF will not bias the results.

We find that majority of the emission at $18.3\mu\text{m}$ comes from region within $2''$ (~ 50 AU) and that $18\mu\text{m}$ emission arises from a spatial extent closer to the star than that of the $24\mu\text{m}$ emission. As shown in Figure 4, we construct a 1-D surface brightness profile of the disk at 18.3 and $24.6\mu\text{m}$. To do so, we exclude the top and bottom 10 rows of pixels to eliminate the background and then sum the flux along the y-axis direction. We find that the $18.3\mu\text{m}$ brightness profiles drops sharply at $\sim 2''$, indicating that the majority of the flux at $18.3\mu\text{m}$ comes from regions within ~ 50 AU. We compare the spatial distribution of $18.3\mu\text{m}$ emission with that of $24.8\mu\text{m}$ by taking the ratio of the two profiles. We find that the $F_{18\mu\text{m}}/F_{24\mu\text{m}}$ flux ratio also drops sharply at $\sim 2''$, indicating that the $18.3\mu\text{m}$ emission is mostly concentrated in the inner ~ 50 AU, while the $24.6\mu\text{m}$ emission is more spread out throughout the disk. The brightness profiles shown in Figure 16 of Ballering et al. (2016) display a similar conclusion.

We estimate the physical location of the grains responsible for the new $\sim 18\mu\text{m}$ emission feature and compare this distance with the semi-major axis (~ 10 AU) of β Pic b. We assume that the dust is optically thin and is in radiative equilibrium. If the dust grains are large, then they will absorb and emit radiation like black bodies and be located at the black body distance. For example, large dust grains at a distance of 9 AU are expected to have a temperature of 160 K and to emit black body radiation whose emission peaks at $\sim 18\mu\text{m}$. However, scattered-light images of debris disks indicate that the black body distance tends to underestimate the actual distance of dust by a factor of ~ 2 (Schneider et al. 2018). Therefore, the grains that are responsible for the $\sim 18\mu\text{m}$ feature are expected to be located at ~ 20 AU. For comparison, the β Pic b planet is located at 10 AU from the star, interior to the dust that produces the feature $18\mu\text{m}$. Given the loose constraints set by the black body distance and the

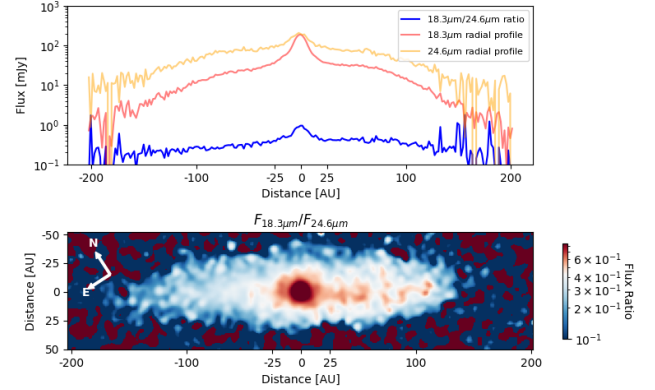


Figure 4. Top: Radial surface brightness profile of the $18.3\mu\text{m}$ band and $24.6\mu\text{m}$ β Pic images from T-ReCS Telesco et al. (2005) imaging and ratio of the surface brightness profile. Bottom: Flux ratio between the $18.3\mu\text{m}$ band and $24.6\mu\text{m}$ from T-ReCS imaging (Telesco et al. 2005). The red color indicates regions in which the $18.3\mu\text{m}$ emission is relatively bright compared with the $24.6\mu\text{m}$ emission. The bottom panel shows that the 18 micron flux originates from regions (red colors) close to central star (within $10''$) while the $24\mu\text{m}$ flux originates from more distant regions in the disk (blue).

Gemini T-ReCS observations, there is still some uncertainty in the relation of the $18\mu\text{m}$ dust distance to the β Pic b planet.

We exclude the possibility that the new $18\mu\text{m}$ feature arises from a halo component. Recent modeling of multi-wavelength β Pic debris disk images (e.g., Ballering et al. 2016) requires the presence of a spatially extended halo ($45\text{ AU--}1800\text{ AU}$ or $\sim 2.25''$ to $90''$) of fine dust grains to reproduce the thermal emission SED. If the $18\mu\text{m}$ feature were generated in the halo, then the spectral feature would have been present in the full slit extraction of the beta Pic spectrum (Chen et al. 2007). However, the full slit extraction does not show an $18\mu\text{m}$ micron feature. Our optimal extraction, on the other hand, weights pixel fluxes by their SNRs in the extraction. In doing so, the extraction heavily weights the emission from the unresolved point source. Specifically, an unresolved point source is expected to have an FWHM of $\sim 1.5''$ at $5\mu\text{m}$ micron and $\sim 7''$ at $24\mu\text{m}$ ($\sim 5''$ at $18\mu\text{m}$). Indeed, at $5\text{--}7.6\mu\text{m}$, the AdOpt extraction window is too small to include the halo; therefore, we rule out the halo contribution to the spectrum at these wavelengths. At longer wavelengths, the extraction window includes increasingly more of the halo until it reaches a maximum FWHM $\sim 12''$ at $40\mu\text{m}$. Even at this longest wavelength, the extraction aperture is not large enough to capture all of the halo flux given the halo geometry from Ballering et al. (2016). Since the full slit extraction did not reveal the new $18\mu\text{m}$ feature, we conclude that the new $18\mu\text{m}$ feature in our optimal extraction spectrum is not due to the halo component in the β Pic disk.

3.4. Tentative Evidence of Weak Infrared Excess around 3–5 μm

In the 5–7 μm region, the *IRS* spectrum is above the stellar photosphere model, indicating a possible excess at 5 μm . The elevated flux in the spectrum is unlikely to be an artifact because the uncertainty in the point-to-point calibration of *IRS* spectra is less than 1%. This 5 μm excess is tentative evidence for the existence of a hot dust population at $\sim 600\text{ K}$ which must be physically located within 0.7 AU to the star. A 5 μm excess has not been previously reported; however, near-infrared interferometric observations have discovered a 0.88% excess at H band (Defrère et al. 2012; Ertel et al. 2014). We used all of the available photometric measurements including WISE W1, W3, W4, and an L band measurement from Bouchet et al. (1991) along with our new IRTF SPEX spectra to determine the onset of the near-infrared excess. As shown in Fig. 2, we find that the L band flux is in good agreement with β Pic’s photosphere model prediction. The lack of infrared excess at 3.77 μm and the infrared excess at 5 μm indicates that there could be a sudden turn-on of infrared excess in that region. This tentative, weak infrared excess indicates that there might be a population of host dust emitting in the wavelength range of 4–5 μm . We discuss the implication of this result in section 6.3.

We find that the 3–5 μm excess is probably due to thermal emission from hot dust. To first order, light that is scattered off of dust grains has the same SED as the stellar host star. Our discovered 3–5 μm excess does not have a color consistent with a Rayleigh-Jeans black body as would be expected for the SED of an A-type star at 3–5 μm . Second, the magnitude of scattered light from the disk is significantly smaller than the observed infrared excess. Even in the brightest cases (STIS scattered light images of debris disks), only $\sim 0.1\%$ of the incident starlight is scattered by the dust (e.g., Schneider et al. 2014). At 5 μm , the *IRS* AdOpt spectrum has a 30% – 50% excess flux with respect to the flux predicted from its stellar photosphere model. Therefore, we exclude the scattered light hypothesis.

4. Spectral Feature Fitting

In this section, our objective is to find the best-fit models of grain properties—composition, size, shape and temperature—for the β Pic AdOpt spectrum. To obtain these properties, we first construct a disk model. Next, we select a suite of lab-measured dust optical constants and use them to calculate dust emissivities by varying grain properties. We then describe our fitting procedure. Finally, we report our best-fit models and immediate findings from these models.

4.1. Modeling Disk Continuum Emission

To isolate the solid state emission from the disk continuum emission, we first model the disk continuum emission

by fitting two black body components to it. As large grains (10–100 μm) mainly contribute to disk continuum emission, most disk continua can be modeled by a two black body model (Mittal et al. 2015). We use 5.61–7.94, 13.02–13.50, 14.32–14.83, 30.16–32.19, and 35.07–35.92 μm regions as anchoring points to fit for two black bodies. We find the disk continuum consists of a warm black body at $\sim 374 \pm 80\text{ K}$ and a cool black body at $\sim 90 \pm 10\text{ K}$ by minimizing the χ^2 value. We plot the two black bodies alongside the disk spectrum in Figure 5. The $\sim 300\text{ K}$ and $\sim 100\text{ K}$ black bodies are later used for estimating the temperatures of the small grains, that are responsible for the solid state emission features. Finally, to obtain a spectrum with only solid state emission features, we subtract the 2 fitted black bodies from the *IRS* photosphere-subtracted β Pic disk spectrum. In the following sections, we work with this version of the spectrum.

4.2. Modeling Solid State Emission Features

We investigate the mass and composition of the silicate grains in the β Pic debris disk by fitting the solid-state features in the *IRS* spectrum. We model the emission from small grains assuming the Rayleigh limit, in which the grain sizes are much smaller than the wavelength of the incident light ($a \ll \frac{\lambda}{2\pi}$). Such small grains are responsible for sharp, well-defined spectral features, while the large grains (in β Pic’s case, 10 μm or larger) can only produce very flat spectral features (e.g., Kessler-Silacci et al. 2006, their Fig. 6, 7, 8). Specifically, for β Pic, past analyses have revealed that sub- μm sub-blowout-sized grains are abundant in the β Pic disk, indicating an active dust replenishing mechanism (e.g., Okamoto et al. 2004; Czechowski & Mann 2007; Dent et al. 2014; Kral et al. 2016). In addition, as these sub- μm -sized grains are expected to be the most abundant grain sizes in β Pic, they dominate the emission cross-sections according to the power-law number distribution (e.g. $f(a) \propto a^{-3.5}$, Dohnanyi 1969; Pan & Schlichting 2012).

To describe the size distribution of these sub- μm -sized grains, we use 3 shape distributions: spheres (Mie theory), a Continuous Distribution of Ellipsoids characterized by equal probability of all shapes (CDE1 hereafter) and by a quadratic weighting in which extreme shapes such as plates and needle have been removed (CDE2) (for the analytical functions of CDE1 and CDE2, see Fabian et al. 2001). The ellipsoids in the CDE distributions can range from prolate ellipsoids such as needles and footballs to oblate ellipsoids such as pancakes and plates. The CDE approximations not only offer analytical solutions for the mass absorption coefficients (MAC), but can also be computed fast enough to quickly explore a large parameter space for different dust compositions at different temperatures and abundances.

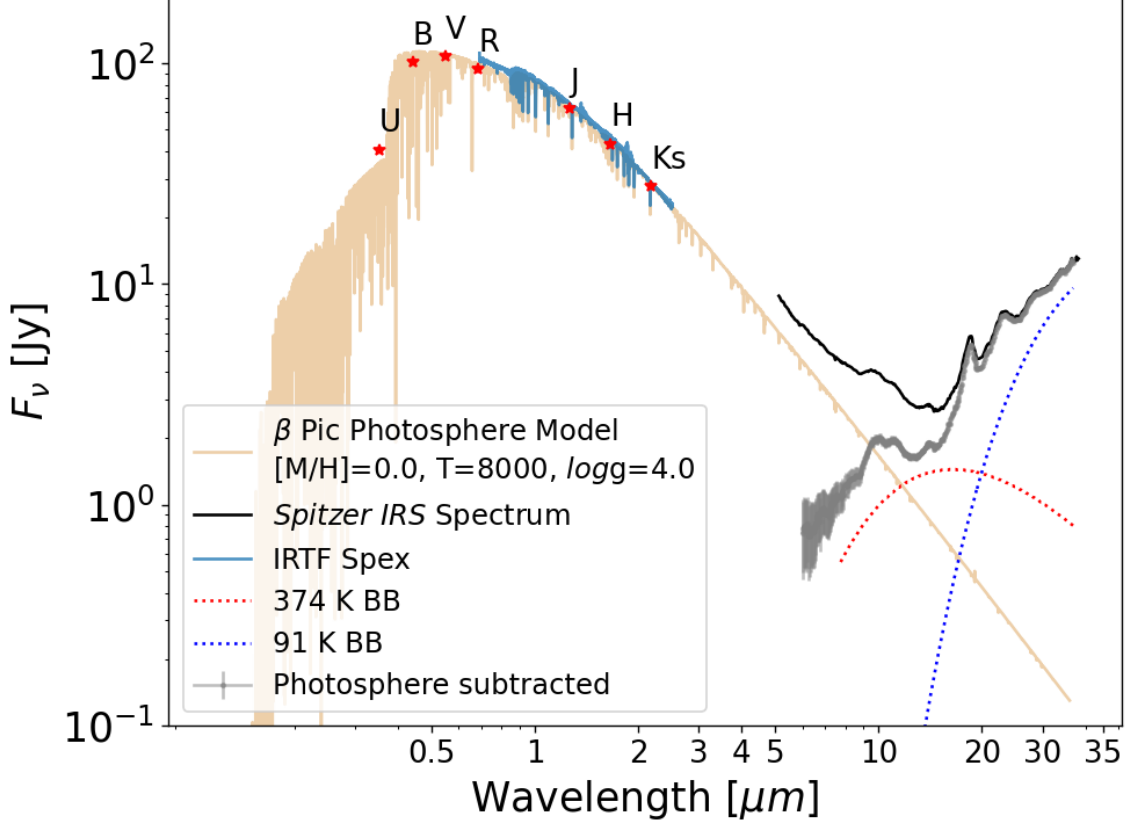


Figure 5. β Pic SED with best fit black bodies overlaid. The cool dust component has a temperature 91K (blue dotted line) while the warm dust component has a temperature 374 K (red dotted line). We use these black body temperatures to select the temperature-dependent forsterite and enstatite optical constants used in our spectral feature fitting.

We assume that the β Pic debris disk is optically thin at all *Spitzer* IRS wavelengths, and therefore the exact solution to the disk model is simply the sum of the emission from each grain population. Previous models have shown that the β Pic system is well-approximated using two thin dust rings, each with distinct composition and temperature (e.g., [Li & Greenberg 1998](#); [Chen et al. 2007](#)). We follow this convention and assume separate temperatures and compositions for each of the two populations. Our model of the disk is similar to that used by ([Sargent et al. 2009a](#)) to model protoplanetary disks,

$$F_\nu = B_\nu(T_c)(a_{c,0} + \sum_i a_{c,i} \kappa_{\nu,i}) + B_\nu(T_w)(a_{w,0} + \sum_j a_{w,j} \kappa_{\nu,j}), \quad (2)$$

where F_ν is the flux at each wavelength, B_ν is the spectral radiance of a black body as a function of temperature, T_c and T_w are the temperatures of the cool and warm components of the disk respectively, and $a_{c,i}$ ($a_{w,j}$) are the mass fraction in which $a_{c,i} = m_{c,i}/d^2$ ($a_{w,j} = m_{w,j}/d^2$). $m_{c,i}$ is the mass of the i^{th} (j^{th}) dust grain species at T_c (T_w) and d is the distance to beta Pic. $a_{c,0}$ and $a_{w,0}$ are offset values that account

for the disk continuum emission from large grains. $\kappa_{\nu,i}$ and $\kappa_{\nu,j}$ are the mass absorption coefficient in $\text{cm}^2 \text{g}^{-1}$ (or emissivity for simplicity). We note that $\kappa_{\nu,i}$ for the crystalline silicate species are temperature dependent but we omit this temperature dependence in the notation.

Our model has a total of 16 free parameters: T_c and T_w , the mass fractions for 6 species of dust grains with temperatures T_c and T_w respectively, and two offset values $a_{c,0}$ and $a_{w,0}$. Table 4 lists the parameters. We model our spectrum by adapting code developed by [Sargent et al. \(2009a\)](#). Since the [Sargent et al. \(2009a\)](#) study, the library of silicate optical constants has grown, expanding to include measurements with a larger number of Fe/Mg ratios and temperatures (e.g., [Zeidler et al. 2015](#)). We tailor the set of optical constants to better fit the β Pic debris disk, leveraging the new laboratory measurements. We require the mass fractions to be non-negative numbers in the fitting procedure and use χ^2 optimization. If the grains were black bodies with the same emissivity, then the two populations would form two concentric thin rings, each with negligible radial width. However, since our model includes 6 different species of dust, where each species has distinct emissivities, grains with different compositions but

the same temperature will not be co-located. The model can be simply understood as a disk with 12 dust rings, with 6 rings emitting at T_c and other 6 emitting at T_w . Note that our choice of emissivities, κ , is limited to lab-measured optical constants at 100 K, but in reality, the cool grains can vary from ~ 80 K to ~ 120 K and their emissivities will change with temperature.

4.3. Dust Emissivity

Past analyses based on spectra and imaging data indicate that grains are predominantly composed of silicates and organics (e.g., [Chen et al. 2007](#); [Ballering et al. 2016](#)). Since the IRS β Pic spectrum shows prominent emission features associated with silicates, we investigate lab-measured optical constants for silicate species. The grain composition primarily affects the central wavelength location of emission features. In addition, for every grain species, four additional grain properties (crystallinity, Fe/Mg ratio, shape, and temperature) can shift the central wavelength features around. Therefore, we explore the Jena database for the most suitable optical constant measurements.

First, we select grain species based on the observed central peak wavelengths and rule out the species from visual examinations. We select olivine and pyroxene, which have characteristic features in the 10, 18–20, 23–25 and 28–33 μm regions. We exclude quartz (SiO_2) as quartz has sharp and triangular 9 μm features that is inconsistent with our trapezoidal 10 μm feature. We also exclude carbonates because our IRS spectra do not have any 6 μm feature that resemble their characteristic features.

Next, we divide the olivine and pyroxene into amorphous and crystalline groups. We use amorphous pyroxene ($\text{Mg}_{0.7}\text{Fe}_{0.3}\text{SiO}_3$) and crystalline pyroxene, which is known as enstatite ([Chihara et al. 2002](#)). We also use amorphous olivine (MgFeSiO_4) from [Dorschner et al. \(1995\)](#) and crystalline olivine, which is known as forsterite from [Zeidler et al. \(2015\)](#); [Fabian et al. \(2001\)](#).¹ Since amorphous grains have only two broad emission features (at 10 μm and 20 μm), their emission features are primarily affected by their size distribution. Therefore, we calculate the emissivities of the small amorphous grains using CDE2 and the emissivities of the large amorphous grains using Mie theory and grains with a 5 μm radius.

For crystalline silicates, there are 3 grain properties that can shift the peak wavelengths of crystalline grain emission features to a shorter wavelength: (1) A decrease in Fe/Mg ratio, (2) a decrease in the grain temperature, and (3) an increase in the grain sizes or porosity. For (1), the peak wavelengths of the emission features shift toward shorter wavelengths as the Fe/Mg ratio decreases, and toward longer

wavelengths as the ratio increases. We show an example in [Figure 6](#) that an 8% increase in the Fe content (from Fo100 to Fo92) broadens and redshifts the bands by 0.18 μm in the 18–20 μm features ([Chihara et al. 2002](#); [Koike et al. 2003](#)).² For (2), the peak wavelength of the emission feature shifts toward a longer wavelength as the temperature of the crystalline silicate increases. For example, a 200 K decrease in forsterite grain temperature (from 300 K to 100 K) would redshift peak wavelength by 0.09 μm from 18.95 to 18.85 μm ([Zeidler et al. 2015](#)). According to our dust continuum model in [Section 4.1](#), we use the 300 and 100 K lab-measured forsterite and enstatite optical constants. Given that [Zeidler et al. \(2015\)](#) measure the optical constants of forsterite and enstatite on a sparse temperature grid of 10, 100, 200, 300, 551, 738 and 928 K, we choose not to interpolate the grid to obtain finer temperature resolutions to avoid introducing artifacts. Even though our best-fit grain temperature might deviate from these exact values by as much as ~ 80 K, we only use the optical constants reported in [Zeidler et al. \(2015\)](#). For (3), as the grain sizes increase or become more porous, the spectral features become flatter for both amorphous and crystalline silicates, and the peak wavelength of the feature shifts towards longer wavelengths ([Kessler-Silacci et al. 2006](#)). To account for the change in grain emission feature due to size and shape effect, we create 3 different shape groups for the same species (see [Table 4](#) “Shape” column) as aforementioned in [Section 4.2](#).

For forsterite, we experiment with the optical constants measured from the San Carlos low-Fe olivine (98.9% Mg-content) sample ([Zeidler et al. 2015](#)) at temperatures from 10K to 928K. We also experiment with the earlier optical constants from [Fabian et al. \(2001\)](#) measured at room temperature. Among all temperatures, we find that the 100 K, 98.9 percent Mg-rich forsterite (Fo99) provides the best wavelength match to the IRS spectrum’s 18.5 μm feature. Interestingly, this Fe/Mg ratio is also consistent with the Fe/Mg ratio (99% Mg) measured from the *Herschel*/PACS 69 μm forsterite band ([de Vries et al. 2012](#)), which is highly sensitive to the Fe/Mg ratio ([Koike et al. 2003](#)). We also include a 300 K Fo90 component for our warm dust component. In addition, we examine the high-Fe content crystalline olivine (known as fayalite) and find that fayalite has double emission peaks in the range of 15–20 μm . We exclude fayalite from our model, because its spectral features are not consistent with our observed single peak emission feature in the same wavelength range.

¹For forsterite and enstatite, we leave their exact stoichiometry for a discussion in the next paragraph.

²Here we use the Fo notation, where Fo stands for the percentage of Fe in forsterite stoichiometry. Fo100 represents the magnesium-rich end-member of olivine, forsterite (Mg_2SiO_4) with 100% Mg and 0% Fe, and Fo0 represents the Fe-rich end-member of olivine, fayalite (Fe_2SiO_4 , known as Fa), with 100% Fe and 0% Mg. For example, Fo80 represents 80% Mg and 20% Fe. The same convention is used to describe the enstatite stoichiometry.

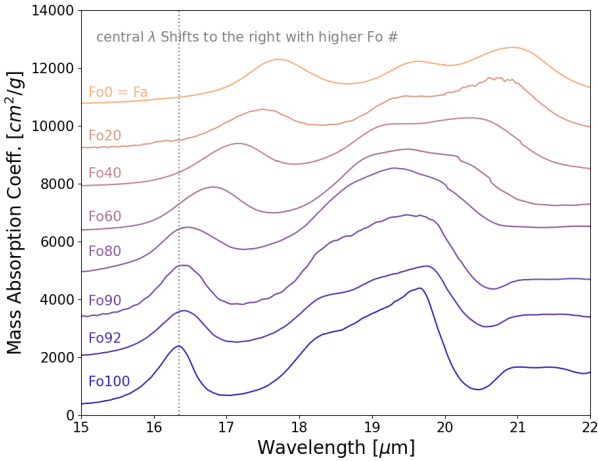


Figure 6. Spectra of forsterite as a function of Fo number at room temperature (~ 300 K). The silicate emission feature central wavelengths shifts towards longer wavelengths with increasing Fe abundance from bottom (Fo100 means 100% Mg and no Fe) to the top (Fa means 100% Fe and no Mg). To help visualize the differences among samples, we vertically offset the spectra, adding multiples of $1000 \text{ cm}^2 \text{ g}^{-1}$ to each spectrum. We note that the emission features vary with both the Fo number and silicate temperature. We fix the temperature at ~ 300 K to showcase the effect of Fo number in this plot.

For enstatite, we use temperature-dependent optical constants from (Zeidler et al. 2015). Similarly, we find that a 98.9% Mg-content enstatite (En99) (Zeidler et al. 2015) at 300 K and 100 K have spectral features that are consistent with our IRS emission features. Therefore, we also include them in our suite of emissivities. We also find that past works (e.g., Sargent et al. 2009a,b) demonstrated that the 95% Mg-content forsterite (Fo95) (Fabian et al. 2001) and 90% Mg-content enstatite (En90) (Chihara et al. 2002) produce good matches with IRS spectra. Therefore, we include an additional set of opacities (Fo95 and En90) as alternative opacities for (Fo99 and En99).

4.4. Fitting Procedures

Based on our black body continuum fit described above, we constrain T_c and T_w to be within (80, 160) and (260, 380) K. Each temperature range is divided into 11 steps and hence the uncertainties for the fit are $\sigma_{T_w} = 7$ K and $\sigma_{T_c} = 10$ K. We minimize χ^2 for our fit by iterating over these two temperature ranges. For a more in-depth description of the fitting procedure, we refer the reader to Section 3.4 in Sargent et al. (2009b) and Section 3.7 in Sargent et al. (2009a).

4.5. Best-Fit Models

We find that β Pic at minimum contains a warm (~ 300 K) and a cool (~ 100 K) population of dust, where the cool population is mainly responsible for the 18–33 μm emission. We plot our best-fit models in Figure 7, 8, 9, and 10 and tabulate their various species of dust masses in Table 4. The best-fit model shows that the 18 μm feature is mostly emitted by the 100 K cool forsterite. The best-fit model contains 3000 times more cool forsterite mass than the 300 K warm forsterite mass.

Even though the 18 μm feature is well modeled in Figure 8, the 23, 28 and 33 μm features are not well modeled. The model-predicted features all have peak wavelengths shorter than the observed peak wavelengths. In Figure 8, gray bands mark the 23, 28 and 33 μm bands where the model does not fit the data well and pale yellow bands showcase where the model performs well.

By modifying our grain shapes to be a moderate continuous distribution of ellipsoids (CDE2), we optimize the fit of the model for the 23 μm spectral feature. Similarly, by modifying our grain shapes to contain extreme shapes in a continuous distribution of ellipsoids (CDE1), we optimize the fit of the model for the 28 and 33 μm spectral features. However, any particular shape distribution (whether spherical, CDE2, or CDE1) only improves the model fit for a localized region (18, 23 or 28&33 μm) in the spectrum. We experiment with a 4-grain model with 4 different temperature components, but find that increasing the number of model parameters does not improve the quality of the fit. The 4-grain model produces a similar χ^2 value ($\chi^2 \approx 26$) to the 2-grain models. Therefore, we report numbers for the 2-grain models. In addition, we also experiment with fitting only an isolated region in the spectrum (instead of the entire spectrum). For example, we fit the 18 μm feature by minimizing only the residual between the model and the data in the 15–20 μm region. However, the model wildly overpredicts the flux in the 10 μm region by more than 200%, sacrificing all other spectral features to optimize one single feature. These undesirable results with alternative models motivate our choice to minimize the residual over the entire wavelength range.

From the dust masses reported in Table 4, we find that the dust population responsible for the 18–33 μm features consists of more than 90% sub- μm -sized crystalline grains and less than 10% of sub- μm -sized amorphous grains in mass. Our best-fit models indicate that the amorphous pyroxene and olivine grains with radii larger than 5 μm cannot account for the solid state emission features in the IRS spectrum. Specifically, in Table 4, the coefficients for “pyroxene (Mie, 5 μm radius, 60% porosity)” and “olivine (Mie, 5 μm radius, 60% porosity)” are all consistent with 0.

Furthermore, for cool dust population, we find that the sub- μm grain shape becomes increasingly irregular with increasing wavelength. For the terrestrial-temperature, warm dust,

Table 4. Dust Masses for the Best-Fit Models of the β Pic debris disk

Species	Shape	10 μm	18 μm	23 μm	28 and 33 μm
		($10^{-3} M_{\text{moon}}$)	($10^{-3} M_{\text{moon}}$)	($10^{-3} M_{\text{moon}}$)	($10^{-3} M_{\text{moon}}$)
Cool Dust Continuum Temperature (T_c)		91 K	84 K	82 K	82 K
Pyroxene ($\text{Mg}_{0.7}\text{Fe}_{0.3}\text{SiO}_3$)	CDE2, Rayleigh Limit	11.6 ± 2.0	0 ± 2.8	0 ± 3.6	0 ± 3.5
Pyroxene	Mie, 5 μm radius, 60% porosity	0 ± 1.5	0 ± 2.2	0 ± 2.7	0 ± 2.7
Olivine (MgFeSiO_4)	CDE2, Rayleigh Limit	10.9 ± 1.5	34.5 ± 2.3	26.0 ± 2.7	19.6 ± 2.6
Olivine	Mie, 5 μm radius, 60% porosity	0 ± 1.0	0 ± 1.4	0 ± 1.8	0 ± 1.7
Forsterite ($\text{Mg}_{1.72}\text{Fe}_{0.21}\text{SiO}_4$)	(1)	3.5 ± 0.8	2514 ± 507	4483 ± 594	3031 ± 425
Enstatite ($\text{Mg}_{0.92}\text{Fe}_{0.09}\text{SiO}_3$)	(1)	0 ± 0.7	183 ± 564	260 ± 250	391 ± 474
Warm Dust Continuum Temperature (T_w)		374 K	298 K	282 K	272 K
Pyroxene ($\text{Mg}_{0.7}\text{Fe}_{0.3}\text{SiO}_3$)	CDE2, Rayleigh Limit	0.019 ± 0.003	0.046 ± 0.006	0.064 ± 0.007	0.067 ± 0.008
Pyroxene	Mie, 5 μm radius, 60% porosity	0 ± 0.003	0.017 ± 0.006	0.031 ± 0.008	0.074 ± 0.009
Olivine (MgFeSiO_4)	CDE2, Rayleigh Limit	0 ± 0.002	0 ± 0.004	0 ± 0.005	0 ± 0.005
Olivine	Mie, 5 μm radius, 60% porosity	0 ± 0.003	0 ± 0.005	0 ± 0.006	0 ± 0.007
Forsterite ($\text{Mg}_{1.72}\text{Fe}_{0.21}\text{SiO}_4$)	(1)	0.0024 ± 0.0017	0.82 ± 0.81	0.82 ± 1.33	0.37 ± 1.46
Enstatite ($\text{Mg}_{0.92}\text{Fe}_{0.09}\text{SiO}_3$)	(1)	0 ± 0.0016	0 ± 0.8	2.3 ± 1.6	1.94 ± 1.69
χ^2	...	23.8	23.6	25.3	30.3

Notes. 1. The shape distribution for forsterite and enstatite are CDE1 for 10 μm feature, Mie for 18 μm feature, CDE2 for 23 μm , CDE1 for 28 and 33 μm features. 2. The warm dust species share the same stoichiometry as the cold dust species. 3. The optical constants for the forsterite and enstatite used for the cool dust are measured at 100 K, while those for the warm dust are measured at 300 K. Therefore, their mass fraction coefficients are independent from each other. 4. The χ^2 values calculated for the best-fit models use the full wavelength range (5–35 μm) in the IRS spectrum.

the 10 μm feature is best-fit using CDE1 grain shapes, which indicates that the grain shapes are irregular. For the cool dust grains, the best-fit models require different grain shape distributions for 18, 23 and 28&33 μm features to optimize the model's χ^2 value. The 18 μm feature is very sharp and is best fitted using spherical grains, while the 23 μm feature is best-fit using CDE2, and the 28 and 33 μm features are best-fit using CDE1.

To conclude, we find that the grain's properties, such as shape, crystallinity, and composition, change with increasing wavelength. In the next section, we examine if there is a trend in silicate crystallinity and Mg/Fe abundance as a function of stellocentric distance, of which wavelength is a proxy.

5. Abundance Analysis

In this section, we investigate whether there is a trend in (1) crystallinity and (2) Fe/Mg in small grains as a function of wavelength, a proxy for stellocentric distance, in the β Pic debris disk. The crystallinity and Fe/Mg ratio inform us about the formation conditions and origins of these silicate dust grains. In section 4, we discover that sub- μm -sized grains are responsible for all prominent 10–33 μm features, where each feature is best fitted by a separate population of grains consisting of both crystalline and amorphous silicates with a distinct mass ratio and a preferential shape distribu-

tion. We group the features by their optimal fits and investigate the properties for each group as a way to probe their parent bodies' properties.

5.1. A Crystallinity Gradient

We investigate crystallinity fractions in small, sub-micron-sized grains as a function of wavelength, as a proxy for radial distances. Note that we do not investigate the crystallinity fraction in large grains with radius equal to or larger than 5 μm , because both amorphous and crystalline grains in this size regime produce very broad and difficult to fit features.

Our model assumes a simplified scenario of grains emitting at two temperatures. If the grains are perfect black bodies from a single population of dust species, then this scenario can be viewed as two concentric, infinitesimally narrow rings. However, our fitting results show that the cold outer belt contains multiple populations of cool forsterite and amorphous silicates that on average emit at ~ 100 K. Hence, this belt must have a non-negligible radial width. To separate the different forsterite populations, we assume the silicates in the disk are in radiative equilibrium and consider grains as black bodies. Then we calculate the black body temperatures that correspond to the peak wavelength of the emission feature with Wien's law and obtain a black body distance. The 10, 18, 23, 28, and 33 μm silicate emission features cor-

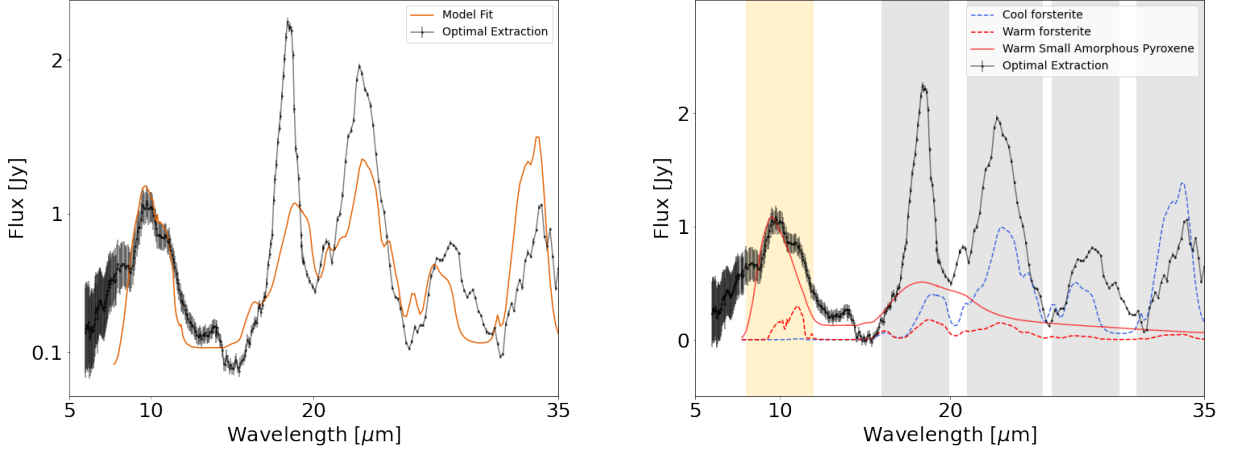


Figure 7. Best-fit model for the $10\ \mu\text{m}$ region. Left: Model fit (orange) plotted over the data (black). Right: Components of different grain species plotted over the data. Warm and cool dust species are plotted in red and blue respectively. Flux from all dust species sums to the model fit (orange) in the left panel. We use gray bands to mark the 18 , 23 , 28 and $33\ \mu\text{m}$ bands where the model does not fit the data well and use pale yellow bands to highlight the areas where the model fits the data well.

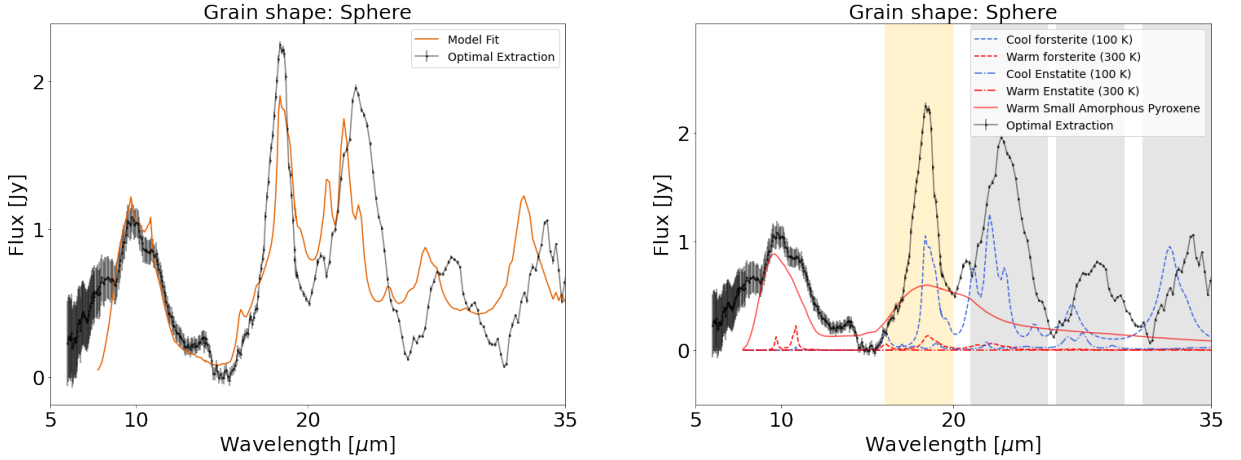


Figure 8. Best-fit model with particle shape calculated with the Mie theory. We show the disk spectrum with its featureless black bodies components subtracted from the total flux. Left: Model fit (orange) plotted over the data (black). Right: Components of different grain species plotted over the data. Warm and cool dust species are plotted in red and blue respectively. Flux from all dust species sums to the model fit (orange) in the left panel. We use gray bands to mark the 23 , 28 and $33\ \mu\text{m}$ bands where the model misfits and use pale yellow bands to showcase where the model performs well.

respond to black body temperatures of 290, 160, 126, 103, and 83 K and radial distances of 3, 9, 14, 21 and 33 AU in the disk, respectively. Note that these distances are lower limits for the actual radial distances, because small grains have lower emission efficiency than black bodies and can stay warm at further radial distances. Note also that our 2-temperature model cannot accurately constrain the temperatures of different cool forsterite populations, as our data is limited to the 100K forsterite opacity.

We use the values in best-fit models at 10 , 18 , 23 , 28 and $33\ \mu\text{m}$ silicate emission features as presented in Fig. 7, 8, 9 and 10 to calculate the abundance of the four silicate species. The crystalline silicate species are enstatite ($\text{Mg}_{0.92}\text{Fe}_{0.09}\text{SiO}_3$) and forsterite ($\text{Mg}_{1.72}\text{Fe}_{0.2}\text{SiO}_4$), and

the amorphous silicate species are olivine and pyroxene. In Fig 11, we calculate the mass percentages of enstatite (green), forsterite (blue), and amorphous silicates (gray) as a function of radial distance.

The crystalline fraction in small grains increases from $14 \pm 3\%$ at $10\ \mu\text{m}$ ($\sim 3\ \text{AU}$) to $99_{-42}^{+1}\%$ at $18\ \mu\text{m}$ ($\sim 10\ \text{AU}$) and remains high from $18\ \mu\text{m}$ ($\sim 10\ \text{AU}$) to $33\ \mu\text{m}$ ($\sim 33\ \text{AU}$). This sudden increase in grain crystallinity at $\sim 10\ \text{AU}$ highlights a major change in the crystallinity of the grain composition. We tabulate the crystallinity fractions in Table 5. Applying these trends to β Pic planetary architecture, we find that the sub-micron-sized silicate grains exterior to the

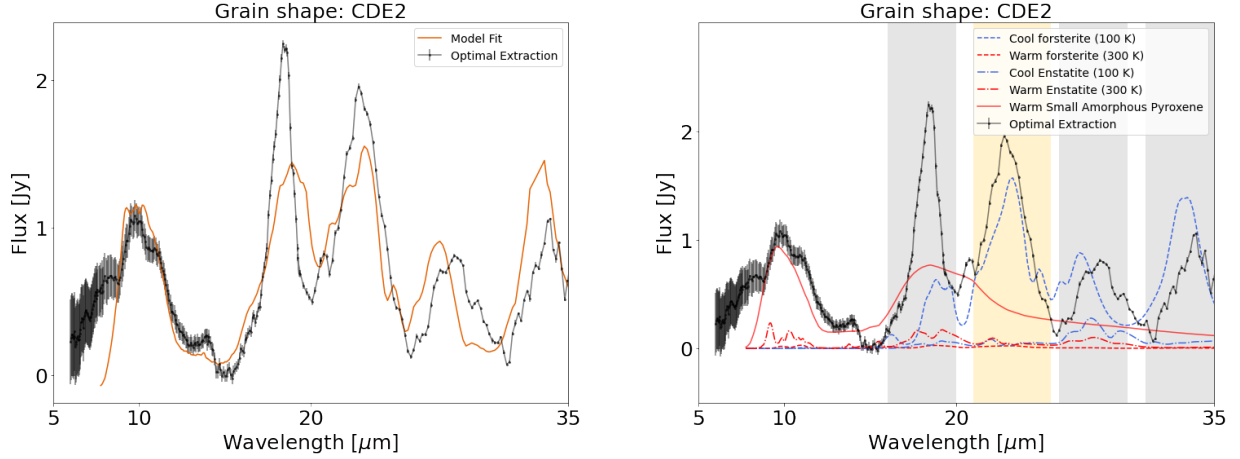


Figure 9. The Best-fit model with particle shape calculated with the continuous distribution of ellipsoids (CDE2, [Fabian et al. 2001](#)) with quadratic weighting for forsterite grains and enstatite grains. We show the disk spectrum with its featureless black bodies components subtracted from the total flux. Left: Model fit (orange) plotted over the data (black). Right: Components of different grain species plotted over the data. The flux from all the grain species (blue and red lines) sums up to the total flux, which equals to the model fit (orange) in the left panel.

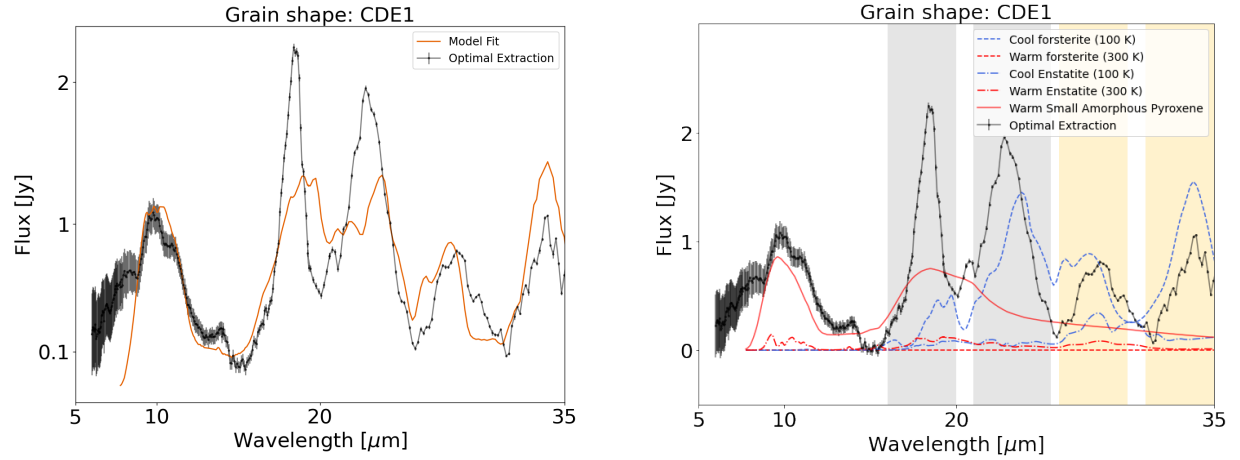


Figure 10. The Best-fit model with particle shape calculated with the continuous distribution of ellipsoids (CDE1, [Fabian et al. 2001](#)) for forsterite grains and enstatite grains by assuming all shapes are equally probable. We show the disk spectrum with its featureless black bodies components subtracted from the total flux. Left: Model fit (orange) plotted over the data (black). Right: Components of different grain species plotted over the data. Warm and cool dust species are plotted in red and blue respectively. Flux from all dust species sums to the model fit (orange) in the left panel

β Pic b (10 AU) are highly crystallized, while the ones interior to β Pic b are mostly amorphous.

To understand the abundance of crystalline grain in the β Pic debris disk, we examine their production mechanisms. Two processes produce crystalline grains in a debris disk: (1) Thermal annealing and (2) collisional grinding between parent bodies with crystalline silicate-rich surfaces. Thermal annealing is a process in which amorphous silicates are heated to high temperatures (but below their vaporization temperatures) for enough time that their internal structure rearranges to be crystal-like, producing forsterite, enstatite, and silica ([Henning 2010](#)). Since thermal annealing is more likely to occur closer to the star, the abundance of crystalline silicates should be the highest closer to the star and decrease with

increasing radial distance. However, we find the opposite trend in crystallinity to that predicted by the thermal annealing scenario, which rules out thermal annealing as the main crystallization mechanism. Alternatively, if the surfaces of the parent bodies are crystalline-rich, continuous collisions among these parent bodies can graze off the surface materials and produce grains with high crystallinity. In our solar system, the A-type asteroids in the main asteroid belt are known to have olivine-dominated surfaces based on their reflection spectra [DeMeo et al. \(2019\)](#). In debris disks, collisional grinding of crystalline-rich parent bodies' surfaces are also thought to generate enstatite-rich dust grains ([Fujiwara et al. 2010](#); [Olofsson et al. 2009](#)). Therefore, the collisional grinding production of crystalline silicates remains a possi-

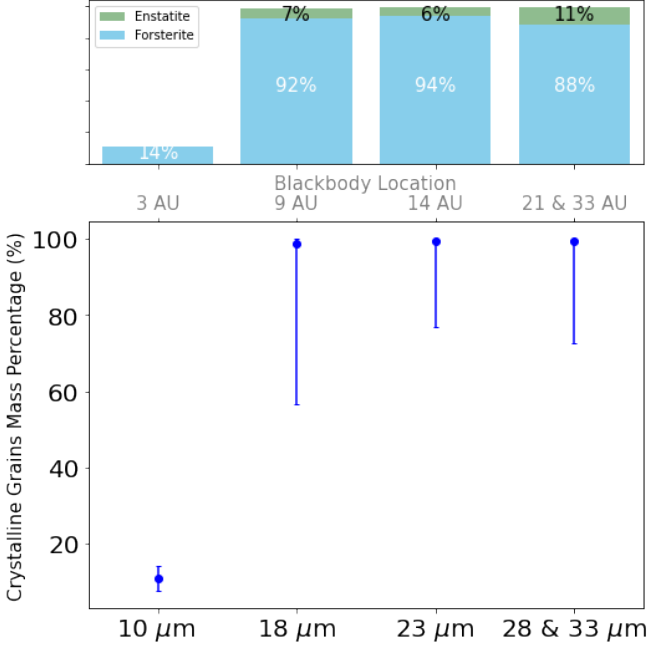


Figure 11. The crystallinity of small silicate grains as a function of radial distance as represented by spectral features emitting at increasing larger disk radii. The y axis shows the percentage of different grain compositions by mass. The x axis shows the best-fit models for 10, 18, 23, 28 and 33 μm silicate features. We calculate a black body distance at each wavelength by assuming that the grains are black bodies and in thermal equilibrium such that the incident stellar radiation on a grain equals to its thermal re-emission. Note that these distances are lower limits to the actual distances where the grains reside because the grain opacity change with wavelength, where the black body’s opacity do not have a wavelength dependence.

ble production mechanism to explain the crystallinity trend in β Pic.

5.2. The Fe/Mg Abundance Ratio as a function of distance

To constrain the formation conditions of the parent bodies in the debris disk, we investigate the Fe/Mg ratio in the crystalline silicates in the disk. We calculate the Fe/Mg ratio by using the silicate masses reported in Table 4 and converting the reported masses into molecular abundance in moles. We then calculate the absolute abundances of Fe and Mg from the stoichiometry of the chemical formulas reported in Table 4. We report the Fe/Mg ratio in Table 5 and plot the Fe/Mg ratio in crystalline silicates as a function of radial distance in Figure 12.

The Fe/Mg ratio remains constant from 10 to 33 μm , but decreases to less than 1% at 69 μm , when we incorporate the Fe/Mg abundance of $(1 \pm 0.1)\%$ measured from *Herschel*/PACS 69 μm forsterite feature (de Vries et al. 2012). Applying this trend to the β Pic planetary architecture, we find that the small dust grains interior to β Pic b (10 AU)

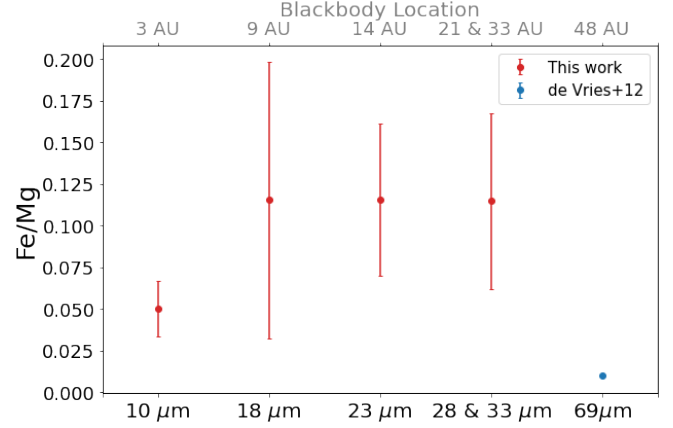


Figure 12. The Fe to Mg ratio for small grains plotted as a function of spectral feature wavelength that can be used as a proxy for stellocentric distance. The red dots with error bars are from this work and the blue dot is the Fe to Mg ratio measured from *Herschel* PACS spectra (de Vries et al. 2012).

are more Fe-rich while the dust grains exterior to β Pic b becomes increasingly Fe-poor. We further discuss the implications of this trend on parent body properties in section 6.1 and 6.2.

In addition, we compare the β Pic’s Fe/Mg ratio with the Fe/Mg ratio measured from white dwarf atmosphere compositions. Recent measurements of precise elemental abundances from white dwarf atmospheres enables us to probe the compositions of extrasolar rocky planetesimals. Interesting, we find that our reported Fe/Mg olivine ratio for the 10 μm warm dust is consistent with that of G29-38 (Xu et al. 2014), suggesting that G29-38’s rocky planetesimals could contain olivine. We also tabulate the Si, O, Mg, and Fe abundances as a function of radial distance (see Table 6). We find that the abundance of all 4 species in small grains increases by a factor of 100 from 22 log(Mole) at 10 μm (~ 300 K) to 24 log(Mole) at 18 μm (~ 160 K).

6. Discussion

6.1. Trends in Silicates and Implications on Parent Body Surface Properties

In section 5, we report our findings that the sub- μm -sized silicate grains are increasingly crystalline, Mg-rich (Fe-poor), and irregular in shape as stellocentric distance increases. We highlight that this critical transition in silicate properties occurs in the vicinity of β Pic b’s orbit. As sub- μm -sized grains must be constantly replenished from planetesimal collisions on orbital timescales, short compared to

Table 5. Fe/Mg Ratio for Crystalline Silicates and Crystallinity Fraction for Grains as a Function of Wavelength

Quantity	10 μm	18 μm	23 μm	28 and 33 μm
Fe/Mg	0.05 ± 0.017	0.12 ± 0.08	0.12 ± 0.05	0.11 ± 0.5
Crystallinity (%)	14 ± 3	99^{+1}_{-42}	$99.5^{+0.5}_{-23}$	$99.5^{+0.5}_{-27}$

Table 6. Element Abundance for the Best-Fit Models of the β Pic debris disk

Species	10 μm	18 μm	23 μm	28 and 33 μm
	[log(Mole)]	[log(Mole)]	[log(Mole)]	[log(Mole)]
Si	22.2 ± 0.7	24.3 ± 0.2	24.5 ± 0.4	24.4 ± 0.4
O	22.8 ± 0.7	24.8 ± 0.2	25.1 ± 0.5	24.9 ± 0.4
Mg	22.2 ± 0.7	24.5 ± 0.3	24.7 ± 0.6	24.6 ± 0.5
Fe	21.9 ± 0.8	23.5 ± 0.3	23.8 ± 0.6	23.6 ± 0.5

the age of the disk, these grains reflect the surface composition and conditions of their parent planetesimals.

From the Fe/Mg trend in silicates, we infer that the surfaces of planetesimals interior to β Pic b are more Fe-rich compared to the surfaces of planetesimals exterior to β Pic b. As Fe-bearing silicates are preferentially produced by planetesimal collisions, as we argue in section 5, the planetesimals close to or interior to β Pic b might have experienced more collisions compared to the planetesimals exterior to β Pic b (outward of 10 AU). If the parent planetesimals have not fully differentiated, then the bulk composition of the planetesimals could be increasingly Fe-poor as stellocentric distance increases.

From the crystallinity trend in silicates, we infer that the surfaces of planetesimals interior to β Pic c (~ 3 AU) are mostly amorphous, while the surfaces of planetesimals exterior to β Pic b are highly crystalline. As crystalline olivine can be easily turned into amorphous olivine via collisions (Henning 2010), the highly crystallized silicate surfaces of planetesimals exterior to β Pic b indicate that these planetesimals have not undergone major collisions.

6.2. Comparing mineralogy of β Pic and Solar System

We compare the Fe/Mg gradient of the β Pic chemical reservoir with that observed in the Solar System. In the Solar System, comets that originate from the Trans Neptunian region contain Mg-rich silicates (Wooden et al. 2017), whereas asteroids and chondrites are Fe-rich (Le Guillou et al. 2015). Such an Fe/Mg trend in the Solar System also leaves imprints on terrestrial planetary surfaces. Specifically, most surfaces

on Mars contain Fo68, an olivine that is relatively Fe-rich, while ancient craters on Mars contains Fo91, which is relatively Fe-poor; Fo91 is thought to originate from the Kuiper belt (Hamilton 2010). Therefore, β Pic and the Solar System share a similar Fe/Mg trend.

We also compare the olivine grain shape distributions in β Pic with the olivine grain sizes observed in our Solar System. In the Solar System, sub- μm -sized forsterite grains are abundant in the chondritic porous interplanetary dust particles (IDP) and comets that originate from the Kuiper belt (Wozniakiewicz et al. 2012), while much larger and less porous forsterite grains are present in asteroids. In contrast, in the β Pic system, we see sub- μm forsterite grains throughout the entire disk; their shapes become increasingly irregular as a function of radial distance. Simulations have shown that the fluffy, irregular grain aggregates can produce qualitatively similar spectral features as porous grains (Kolokolova & Kimura 2010). If we consider grain shape a proxy for grain porosity, then the sub- μm -sized, irregular forsterite grains in the outskirts of the β Pic disk correspond to the forsterite grains in our Solar System’s comets and IDP.

Our discovery of these similarities paves the way for future space-based spatially-resolved MIR spectroscopy studies. Higher spatial resolution observation of JWST will improve our understanding of β Pic’s planetary system architecture. Future JWST GTO (ID: 1294) observations will be able to probe the spatial distribution of the the forsterite population with an improved resolution (by a factor of ~ 10 in spatial resolution compared to Spitzer’s spital resolution) with the MIRI Medium Resolution Spectroscopy as well

as a higher overall SNR (compared to ground-based high-resolution observations). The Gemini T-ReCS images revealed an asymmetric dust distribution at $18.3\ \mu\text{m}$ in the disk (Telesco et al. 2005), while the *Spitzer* discovery provides complimentary spectroscopic information by pinpointing the $18\ \mu\text{m}$ forsterite emission which give good constraints on grain properties such as Fe/Mg and crystallinity and shape. JWST would be able to map and compare the size, shape and mass distributions of cool forsterite grains in the southwest and northeast side of the disk, leveraging the knowledge from Gemini and *Spitzer*. The future JWST MRS observations will also potentially resolve more solid state emission features and therefore refine measurements of Fe/Mg and crystallinity ratio for the $18\text{--}33\ \mu\text{m}$ features.

6.3. Tentative Evidence for Weak $3\text{--}5\ \mu\text{m}$ Hot Dust

In section 3.4, we show that a population of $\sim 600\ \text{K}$ hot dust population located within $0.7\ \text{AU}$ likely contributes to $\sim 50\%$ of excess flux at around $3\text{--}5\ \mu\text{m}$. In comparison, past H and K band interferometric measurements indicate a $\sim 1500\ \text{K}$ hot dust population located at least within $4\ \text{AU}$ to the star (Ertel et al. 2014; Defrère et al. 2012). It is uncertainty whether the tentative $\sim 600\ \text{K}$ hot dust is related to the $\sim 1500\ \text{K}$ hot dust population. The $\sim 600\ \text{K}$ hot dust could have multiple origins. ALMA dust continuum images (e.g., Kral et al. 2016) have shown that the inner disk does not have obvious cavity and can still contain abundant small planetesimals to produce the $\sim 600\ \text{K}$ hot dust. Alternatively, inward P-R drag could operate to move the $10\ \mu\text{m}$ warm dust grains into inner region of the disk. It is also possible that there are stochastic events in the inner region of the disk such as comets infalling activities (Kiefer et al. 2014) could produce the $\sim 600\ \text{K}$ hot dust population. Future observations are needed to confirm the tentative $\sim 600\ \text{K}$ hot dust population. β Pic is too bright to be observed by JWST from space but can be observed from the ground. IRTF is a suitable facility for obtaining the $2.5\text{--}5\ \mu\text{m}$ NIR spectrum with high SNR to constrain the level of hot dust excess in this system.

7. Conclusion

We re-analyze the *Spitzer* IRS data of the β Pic debris disk with AdOpt (Lebouteiller et al. 2010). To better constrain the stellar parameters, we obtain a new NASA IRTF SpeX spectrum from $0.7\text{--}3\ \mu\text{m}$ and found a weak $3\text{--}5\ \mu\text{m}$ excess possibly due to hot dust close to the star. We discover a prominent $18\ \mu\text{m}$ silicate feature for the first time and an enhanced $23\ \mu\text{m}$ feature. These narrow spectroscopic features placed good constraints on grain properties such as Fe/Mg ratio, crystallinity and shape. We find that the $\sim 100\ \text{K}$ forsterite grains are the main contributors to these two features. Furthermore, we find three trends in grain properties as functions of wavelengths: (1) The Fe/Mg ratio in silicates

decreases with stellocentric distances. We infer that the surface composition of the planetesimals is increasingly Mg-rich and pristine the further away they are from the star. We find β Pic’s chemical gradient offers an analogy to our Solar System’s clearly divided grain chemical reservoirs; (2) the grains become more crystalline with increasing wavelengths and (3) lastly, the grain shapes become increasing irregular with increasing wavelengths. The findings imply that the properties of dust population in the vicinity of β Pic b and c differs significantly in crystallinity, shape and Fe/Mg ratio. This is the first time that such a trend in spectral features has been studied with space-based MIR spectroscopy for a debris disk. Future JWST MIRI observations will constrain the spatial location of the grains that are responsible for the newly discovered 18 and $23\ \mu\text{m}$ spectral features and probe β Pic b’s atmospheric cloud composition for comparison with dust properties in the planet’s vicinity.

We thank Alycia Weinberger, Benjamin Montesinos, Francisca Kemper, John Debes, Roc Cutri, Bin Ren and Jingwen Fan for useful discussions. CL acknowledges support from STScI Director’s Research Fund (DRF) and NASA FINESST grant. This work is supported by the National Aeronautics and Space Administration under Grant No. 80NSSC21K1844 issued through the Mission Directorate. This work is based on archival data obtained with the Spitzer Space Telescope, which was operated by the Jet Propulsion Laboratory, California Institute of Technology under a contract with NASA. This research has made use of the NASA/IPAC Infrared Science Archive, which is funded by the National Aeronautics and Space Administration and operated by the California Institute of Technology. This publication makes use of data products from the Wide-field Infrared Survey Explorer, which is a joint project of the University of California, Los Angeles, and the Jet Propulsion Laboratory/California Institute of Technology, and NEOWISE, which is a project of the Jet Propulsion Laboratory/California Institute of Technology. WISE and NEOWISE are funded by the National Aeronautics and Space Administration. This research has made use of NASA’s Astrophysics Data System. This research has made use of the SIMBAD database, operated at CDS, Strasbourg, France (Wenger et al. 2000). This research has made use of the VizieR catalogue access tool, CDS, Strasbourg, France (DOI: 10.26093/cds/vizie). The original description of the VizieR service was published in 2000, A&AS 143, 23 (Ochsenbein et al. 2000).

Appendix A. Spitzer IRS Spectrograph Slit Orientation

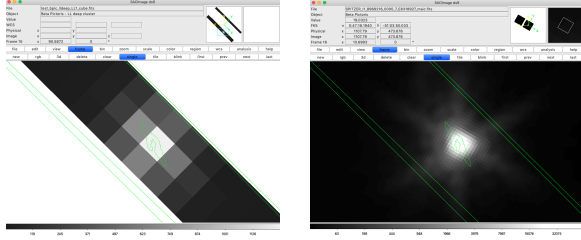


Figure A1. The β Pic debris disk in the slit of IRS spectrograph. The coordinate display here is the world coordinate system (WCS), in which North points upwards and East points to the left. The green contour shows the disk of β Pic in scattered light, and is obtained from the scattered light image with the Space Telescope Imaging Spectrograph (STIS) on the Hubble Space Telescope (HST) (Ren et al. 2017, See Figure 6c therein.). The South-West side of the disk contains a gas clumps as seen in ALMA. The disk is measured to have a position angle of $PA_{\text{disk}} = 29.51^\circ$. The edges of the IRS spectrograph slit indicated by the green lines (we zoom in to show part of the slit, since the entire slit is too long). The slit has a position angle of $PA_{\text{slit}} = 44.97 \pm 0.02^\circ$. The disk is 15° misaligned with respect to the slit. Left: The mosaic image in the background is the β Pic 2D spectral map taken with IRS Long-low 1 (LL1) mode and assembled using `Cubism` (Sings IRS Team et al. 2011). Shown here is the disk at $20.52 \mu\text{m}$, and there are 100 other slices (not shown here) in LL1 that span $\lambda \sim 20 \mu\text{m}$ to $39 \mu\text{m}$ in wavelength. The disk roughly spans 2.5 pixels in this image and each pixel is square with $5.1''$ on each side. Right: The background image is taken with *Spitzer* MIPS $24 \mu\text{m}$ image. The image pixel has the size of $2.49'' \times 2.60''$. We use MIPS photometry for absolute flux calibration for the IRS spectrum.

References

- Allard, F., Homeier, D., & Freytag, B. 2012, *RSPTA*, 370, 2765
- Ballering, N. P., Su, K. Y. L., Rieke, G. H., & Gáspár, A. 2016, *ApJ*, 823, 108
- Bonnefoy, M., Boccaletti, A., Lagrange, A. M., et al. 2013, *A&A*, 555, A107
- Bouchet, P., Manfroid, J., & Schmider, F. X. 1991, *A&AS*, 91, 409
- Brownlee, D. 2008, *Physics Today*, 61, 30
- Chen, C. H., Mittal, T., Kuchner, M., et al. 2014, *ApJS*, 211, 25
- Chen, C. H., Su, K. Y. L., & Xu, S. 2020, *NatAs*, 4, 328
- Chen, C. H., Li, A., Bohac, C., et al. 2007, *ApJ*, 666, 466
- Chihara, H., Koike, C., Tsuchiyama, A., et al. 2002, *A&A*, 391, 267
- Claret, A. 2000, *A&A*, 363, 1081
- Claret, A., Diaz-Cordoves, J., & Gimenez, A. 1995, *A&AS*, 114, 247
- Cushing, M. C., Vacca, W. D., & Rayner, J. T. 2004, *PASP*, 116, 362
- Cutri, R. M., & et al. 2012, *VizieR Online Data Catalog*, II/311
- Czechowski, A., & Mann, I. 2007, *ApJ*, 660, 1541
- de Vries, B. L., Acke, B., Blommaert, J. A. D. L., et al. 2012, *Nature*, 490, 74
- Defrère, D., Lebreton, J., Le Bouquin, J. B., et al. 2012, *A&A*, 546, L9
- DeMeo, F. E., Polishook, D., Carry, B., et al. 2019, *Icarus*, 322, 13
- Dent, W. R. F., Wyatt, M. C., Roberge, A., et al. 2014, *Science*, 343, 1490
- Dohnanyi, J. S. 1969, *JGR*, 74, 2531
- Dorschner, J., Begemann, B., Henning, T., et al. 1995, *A&A*, 300, 503
- Ducati, J. R. 2002, *VizieR Online Data Catalog*, II/237
- Ertel, S., Absil, O., Defrère, D., et al. 2014, *A&A*, 570, A128
- Fabian, D., Henning, T., Jäger, C., et al. 2001, *A&A*, 378, 228
- Fujiwara, H., Onaka, T., Ishihara, D., et al. 2010, *ApJL*, 714, L152
- Guess, A. W. 1962, *ApJ*, 135, 855
- Hamilton, V. E. 2010, *Geochemistry*, 70, 7
- Hauschildt, P. H., Allard, F., & Baron, E. 1999, *ApJ*, 512, 377
- Henning, T. 2010, *ARA&A*, 48, 21
- Higdon, S. J. U., Devost, D., Higdon, J. L., et al. 2004, *PASP*, 116, 975
- Houck, J. R., Roellig, T. L., van Cleve, J., et al. 2004, *ApJS*, 154, 18
- Hughes, A. M., Duchêne, G., & Matthews, B. C. 2018, *ARA&A*, 56, 541
- Kessler-Silacci, J., Augereau, J.-C., Dullemond, C. P., et al. 2006, *ApJ*, 639, 275
- Kiefer, F., Lecavelier des Etangs, A., Boissier, J., et al. 2014, *Nature*, 514, 462
- Koike, C., Chihara, H., Tsuchiyama, A., et al. 2003, *A&A*, 399, 1101
- Kolokolova, L., & Kimura, H. 2010, *Earth, Planets and Space*, 62, 17
- Kral, Q., Wyatt, M., Carswell, R. F., et al. 2016, *MNRAS*, 461, 845
- Lagrange, A. M., Gratadour, D., Chauvin, G., et al. 2009, *A&A*, 493, L21
- Lagrange, A. M., Bonnefoy, M., Chauvin, G., et al. 2010, *Science*, 329, 57
- Lagrange, A. M., Rubini, P., Nowak, M., et al. 2020, *A&A*, 642, A18
- Larwood, J. D., & Kalas, P. G. 2001, *MNRAS*, 323, 402
- Le Guillou, C., Changela, H. G., & Breatley, A. J. 2015, *Earth and Planetary Science Letters*, 420, 162
- Lebouteiller, V., Bernard-Salas, J., Sloan, G. C., & Barry, D. J. 2010, *PASP*, 122, 231
- Li, A., & Greenberg, J. M. 1998, *A&A*, 331, 291
- Lisse, C. M., Kraemer, K. E., Nuth, J. A., et al. 2007, *Icarus*, 187, 69
- Lisse, C. M., VanCleve, J., Adams, A. C., et al. 2006, *Science*, 313, 635
- Lytle, D., Stobie, E., Ferro, A., & Barg, I. 1999, *Astronomical Society of the Pacific Conference Series*, 172, 445
- Mainzer, A., Bauer, J., Grav, T., et al. 2011, *ApJ*, 731, 53
- Mermilliod, J. C., Mermilliod, M., & Hauck, B. 1997, *A&AS*, 124, 349
- Mittal, T., Chen, C. H., Jang-Condell, H., et al. 2015, *ApJ*, 798, 87
- Morales, F. Y., Padgett, D. L., Bryden, G., et al. 2012, *ApJ*, 757, 7
- Nowak, M., Lacour, S., Lagrange, A. M., et al. 2020, *A&A*, 642, L2
- Ochsenbein, F., Bauer, P., & Marcout, J. 2000, *A&AS*, 143, 23
- Okamoto, Y. K., Kataza, H., Honda, M., et al. 2004, *Nature*, 431, 660
- Olofsson, J., Augereau, J. C., van Dishoeck, E. F., et al. 2009, *A&A*, 507, 327
- Pan, M., & Schlichting, H. E. 2012, *ApJ*, 747, 113
- Pecaut, M. J., & Mamajek, E. E. 2013, *ApJS*, 208, 9
- Rayner, J. T., Toomey, D. W., Onaka, P. M., et al. 2003, *PASP*, 115, 362
- Reach, W. T., Vaubailon, J., Lisse, C. M., et al. 2010, *Icarus*, 208, 276
- Ren, B., Pueyo, L., Perrin, M. D., et al. 2017, *Proc. SPIE*, 10400, 1040021
- Sargent, B. A., Forrest, W. J., Tayrien, C., et al. 2009a, *ApJS*, 182, 477
- . 2009b, *ApJ*, 690, 1193
- Schneider, G., Grady, C. A., Hines, D. C., et al. 2014, *AJ*, 148, 59
- Schneider, G., Debes, J. H., Grady, C. A., et al. 2018, *AJ*, 155, 77
- Sings IRS Team, Smith, J. D., Armus, L., et al. 2011, *CUBISM: CUBE Builder for IRS Spectra Maps*
- Sloan, G. C., Herter, T. L., Charmandaris, V., et al. 2015, *AJ*, 149, 11
- Su, K. Y. L., Rieke, G. H., Stansberry, J. A., et al. 2006, *ApJ*, 653, 675
- Telesco, C. M., Fisher, R. S., Wyatt, M. C., et al. 2005, *Nature*, 433, 133
- Vacca, W. D., Cushing, M. C., & Rayner, J. T. 2003, *PASP*, 115, 389
- Wahhaj, Z., Koerner, D. W., Ressler, M. E., et al. 2003, *ApJL*, 584, L27
- Weinberger, A. J., Becklin, E. E., & Zuckerman, B. 2003, *ApJL*, 584, L33
- Wenger, M., Ochsenbein, F., Egret, D., et al. 2000, *A&AS*, 143, 9
- Wooden, D. H., Ishii, H. A., & Zolensky, M. E. 2017, *RSPTA*, 375, 20160260
- Wozniakiewicz, P. J., Bradley, J. P., Ishii, H. A., et al. 2012, *ApJL*, 760, L23
- Wright, E. L., Eisenhardt, P. R. M., Mainzer, A. K., et al. 2010, *AJ*, 140, 1868
- Xu, S., Jura, M., Koester, D., et al. 2014, *ApJ*, 783, 79
- Zeidler, S., Mutschke, H., & Posch, T. 2015, *ApJ*, 798, 125